

# HUBBLE SPACE TELESCOPE FAINT OBJECT SPECTROGRAPH OBSERVATIONS OF A UNIQUE GROUPING OF FIVE QSOs: THE SIZES AND SHAPES OF LOW- $z$ Ly $\alpha$ FOREST ABSORBERS<sup>1</sup>

ERIC M. MONIER,<sup>2</sup> DAVID A. TURNSHEK, AND CYRIL HAZARD

Department of Physics and Astronomy, University of Pittsburgh, Pittsburgh, PA 15260; monier@astronomy.ohio-state.edu, turnshek@vms.cis.pitt.edu, hazard@vms.cis.pitt.edu

Received 1999 January 18; accepted 1999 April 21

## ABSTRACT

Observations of QSO pairs suggest that the structures responsible for Ly $\alpha$  forest absorption lines must have radii of hundreds of kiloparsecs if they are spherical or disklike in shape. However, only observations of groups of three or more QSOs closely spaced on the sky provide a way to measure their transverse sizes/characteristic clustering lengths *and* shapes. Such observations are needed to test the predictions of cosmological simulations of large-scale structure formation. To further this goal, we have obtained *Hubble Space Telescope* Faint Object Spectrograph G190H spectra of a grouping of five QSOs to investigate the sizes and shapes of absorbers at a redshift of  $z \approx 0.7$ . The angular separations of the pairs in this unique configuration range from  $1' - 8'$ , for which the corresponding lines of sight probe proper separations as small as  $200 h^{-1}$  kpc and up to  $2 h^{-1}$  Mpc. The redshifts of the four quasars with detected flux in the observed region of  $1700 - 2300 \text{ \AA}$  are  $z = 0.86, 1.01, 1.01, \text{ and } 1.10$ . In the pair with the smallest separation (0.98), six greater than  $4.5 \sigma$  Ly $\alpha$  line pairs are found in common (within  $150 \text{ km s}^{-1}$ ) between the two lines of sight, significant above the random background at the 99.2% level. In the QSO pairs with larger separations, the number of lines in common is consistent with the chance expectation determined from Monte Carlo simulations. The results imply that an upper limit to the absorber sizes is crossed in the interval between the two smallest separation pairs. In addition, we find evidence that the exclusion of weaker lines results in smaller absorber sizes. Using results from a  $4.5 \sigma$  sample of lines in the QSO pair with the smallest separation, we estimate the sizes of simple spherical and thin-disk absorbers using a Bayesian analysis and find a most likely radius of  $159 h^{-1}$  kpc and a 95% confidence interval of  $135 < R < 218 h^{-1}$  kpc for spheres, and a most likely radius of  $196 h^{-1}$  kpc and a 95% confidence interval of  $157 < R < 289 h^{-1}$  kpc for disks. We also model filamentary structures as cylinders and compare the simulated behavior of these cylinders with the observed occurrence of pairs in the three smallest separation pairs. We find that cylinders of  $R \approx 130 - 200 h^{-1}$  kpc and few Mpc long could be expected to produce the observed behavior of the Ly $\alpha$  lines in these QSO pairs and note that these dimensions are in good agreement with the sizes of filamentary structures (or segments thereof) predicted by numerical simulations of large-scale structure at low redshifts. The overall results demonstrate that observations of QSO groups can be used to derive information on the sizes *and* shapes of absorbing material in the intergalactic medium, providing insight into the evolution of gas and galaxies in the universe.

*Subject headings:* intergalactic medium — quasars: absorption lines — quasars: general

## 1. INTRODUCTION

Intervening Ly $\alpha$  and metal absorption lines in QSO spectra have proved to be powerful tools for investigating structure in the universe. Their utility is somewhat limited along single lines of sight, however, in that they provide no information about the transverse extent of the absorbers, and no measurement of the kinematics or spatial scales perpendicular to the line of sight is possible. Pairs and groups of QSOs having small angular separations provide a way to measure the transverse sizes, characteristic clustering lengths, and shapes of the structures responsible for Ly $\alpha$  forest absorption. Observations that search for common or correlated Ly $\alpha$  absorption along the additional, adjoining lines of sight over a range of length scales offer one of the few direct approaches to constraining models of Ly $\alpha$  forest absorbers. At one extreme, dense clouds that are

not very highly ionized will produce common absorption only on the smallest scales but might still be correlated on larger scales over small velocity intervals if there is clustering, while more tenuous, highly ionized clouds may produce common absorption over very large length scales. The use of gravitationally lensed and physical pairs of QSOs to place constraints on the sizes and velocity characteristics of the various types of intervening absorbers has been gaining momentum in recent years, due in part to *Hubble Space Telescope* (HST) and its ability to observe the Ly $\alpha$  forest below  $z \approx 1.7$  and to resolve the individual components of gravitational lenses.

Studies of gravitationally lensed QSOs separated by a few arcseconds probe structure on subgalactic scales (Weymann & Foltz 1983; Foltz et al. 1984; Smette et al. 1992, 1995; Bechtold & Yee 1994; Petry, Impey, & Foltz 1998; Monier, Turnshek, & Lupie 1998). With enough wavelength coverage of the Ly $\alpha$  forest, the correlation seen in the equivalent widths of the Ly $\alpha$  lines between the lines of sight is very strong at the smallest separations, suggesting that the lines of sight are passing through the same absorbers and providing a lower limit on their size. At slightly larger separations (i.e., tens of arcseconds), some

<sup>1</sup> Based on observations with the NASA/ESA *Hubble Space Telescope*, obtained at the Space Telescope Science Institute, which is operated by AURA, Inc., under NASA contract NAS 5-26555.

<sup>2</sup> Current address: Ohio State University, Department of Astronomy, 174 West 18th Street, Columbus, OH 43210.

$\text{Ly}\alpha$  absorption lines still appear to be common to both lines of sight, but complete correlation is no longer seen. At this point, upper limits on the sizes of absorbers with simple shapes can be estimated as well and are on the order of hundreds of kiloparsecs (Bechtold et al. 1994; Dinshaw et al. 1994; Petitjean et al. 1998). Investigations of pairs separated by  $\approx 1'$  still find  $\text{Ly}\alpha$  lines in common between lines of sight (Shaver & Robertson 1983; Dinshaw et al. 1995, 1997, hereafter D97; D'Odorico et al. 1998) that may not be due to large, individual absorbers but rather clustered associations of smaller ones. At slightly larger separations (i.e., a few arcminutes) the results are conflicting, and examples exist of both no (or little) correlation (Sargent, Young, & Schneider 1982; Elowitz, Green, & Impey 1995; Dinshaw et al. 1998) and strong correlation (Crotts 1989; Fang et al. 1996; Crotts & Fang 1998). Finally, it seems clear from studies of the  $\text{Ly}\alpha$  forest using wide-separation ( $\geq 1^\circ$ ) QSOs that no evidence for common or correlated absorption will be found on scales of tens of megaparsecs (e.g., Elowitz et al. 1995), although there are indications of correlations in the metal-line systems on supercluster size scales in the case of the Tololo pair (Jakobsen et al. 1986; Dinshaw & Impey 1996).

Since there are relatively few pairs and groups of QSOs known, these studies have in many cases used the same sets of QSOs, occasionally obtaining different results. It is therefore desirable to populate the gap between complete correlation and no correlation with as many additional QSO pairs as possible having separations in the range between. In addition, observations along *multiple* (i.e., more than two) sightlines are needed to constrain the actual shapes of absorbers on all scales, since observations of groups of more than two QSOs will probe multiple size scales in the same region. This is particularly important if the clouds are in the form of sheets or filaments, as suggested by numerical simulations of large-scale structure at moderate to high redshifts (see, e.g., Miralda-Escudé et al. 1996; Charlton, Churchill, & Linder 1995; Charlton et al. 1997; Cen & Simcoe 1997; Davé et al. 1999).

Furthermore, observations over a range of redshifts will be required to develop a clear picture of the evolution of large-scale structure, particularly during the epoch of galaxy formation. While current estimates of absorber sizes are spread over a range of scales and redshifts, most are from ground-based observations and therefore correspond to  $z > 1.7$ . Of the three physical QSO pairs observed so far with *HST*, only the lines of sight toward Q0107–095A,B have been studied down to redshifts as low as  $z \approx 0.5$  (Dinshaw et al. 1995; D97). Observations at the lower redshifts can test, for example, the possibility that the stronger  $\text{Ly}\alpha$  lines at  $z < 1$  arise in the extended halos of galaxies (Lanzetta et al. 1995; Chen et al. 1997). In addition, the redshift aspect is important because it is generally accepted that clustering will increase at lower redshift, and any galaxy merger scenario would, of course, result in the growth of large structures. Low redshift superclusters have length scales greater than 10 Mpc. Moreover, results from the *HST* Quasar Absorption Line Key Project (Bahcall et al. 1993, 1996, hereafter CAT2; Weymann et al. 1998) suggest that there may be a change in the evolution of the  $\text{Ly}\alpha$  forest cloud population at  $z \approx 1.0$ –1.5, with the number of clouds decreasing less rapidly at low redshift than at high redshift. There has been speculation, in fact, that a new population of  $\text{Ly}\alpha$  clouds is emerging at lower redshift, with

the lower redshift population being closely associated with galaxies, while the high-redshift population evolves more rapidly and is unclustered. About half of the extensive metal-line systems being found at lower redshift ( $z \approx 0.5$ –1.0) in the Key Project are accompanied by clumps of  $\text{Ly}\alpha$  lines with velocity dispersions of  $\approx 600$ –1400 km s $^{-1}$ . If interpreted as a Hubble flow, this velocity corresponds to dimensions of  $\approx 4$ –9  $h^{-1}$  Mpc.<sup>3</sup> In view of recent results, therefore, it is important to perform direct searches for common absorption or clustering of  $\text{Ly}\alpha$  systems on a wide range of scales so that direct constraints can be applied to the lower redshift population of  $\text{Ly}\alpha$  clouds.

The four QSOs discovered by Hazard, Arp, & Morton (1979) all lie within  $4'$  of each other on the sky. A fifth radio-loud QSO possessing a  $z_{\text{abs}} \approx z_{\text{em}}$  system, MC 1146+111 (QSO “E”), is within  $8'$  of A, B, C, and D. All five QSOs were bright enough for observation with *HST*-FOS, offering an unprecedented chance to investigate the behavior of the  $\text{Ly}\alpha$  forest at low redshift over separations ranging from 200  $h^{-1}$  kpc to 2  $h^{-1}$  Mpc. [The QSOs subsequently appeared in Arp & Hazard (1980), with the unfortunate consequence that they were labeled slightly differently than in Hazard et al. (1979). For the sake of brevity, we adopt the labeling convention of Hazard et al. in their Fig. 1 (alternate names follow in parentheses): QSO A (H1146+111B), QSO B (H1146+111E), QSO C (H1146+111C), QSO D (H1146+111D), and QSO E (MC 1146+111)]. The redshifts of the QSOs are  $z_{\text{em}} = 1.01, 1.10, 1.01, 2.12$ , and  $0.86$ , respectively. The grouping initially received a great deal of attention (e.g., Paczyński 1986; Turner et al. 1986; Phinney & Blandford 1986; Shaver & Cristiani 1986; Ostriker & Vishniac 1986; Huchra 1986; Silk 1986; Blandford, Phinney, & Narayan 1987), and issues involving binary clustering, binary quasars, and gravitational lensing have been discussed.

In this paper, we use *HST*-FOS G190H observations of these QSOs to place constraints on the sizes and shapes of the  $\text{Ly}\alpha$  absorbers over  $0.4 < z_{\text{abs}} < 0.9$ . The results are dominated by the closest separation pair of QSOs, A and B, in which a moderate correlation detected between the lines of sight decreases with the equivalent width of the sample considered. No convincing evidence exists for any correlation in the QSO pairs at the next largest separation and beyond. The findings support the hypothesis of large absorbers, though not as large as those estimated by D97. We derive sizes assuming simple geometries of spheres and inclined disks and find that the radii inferred from the behavior of disks are consistent with the impact parameter,  $b = 160 h^{-1}$  kpc, estimated by Lanzetta et al. (1995) and Chen et al. (1997) for absorption by low- $z$  galaxies.

The observations are described in § 2, and the steps taken to analyze the spectra and form the absorption-line lists are detailed in § 3. In § 4 we describe several samples used to evaluate the presence of correlations between pairs of lines of sight and compare the equivalent widths in the line pairs. The results of § 4 are used to estimate the sizes of the clouds assuming simple spherical and thin-disk geometries in § 5. We also set limits on the dimensions of possible filamentary structures. In § 6, the findings are summarized, and we discuss implications for models of the  $\text{Ly}\alpha$  forest and the predictions of cosmological simulations.

<sup>3</sup> The present-day Hubble constant  $H_0$  is defined in terms of  $h$ , where  $H_0 = 100 h \text{ km s}^{-1} \text{ Mpc}^{-1}$ .

TABLE 1  
JOURNAL OF *HST*-FOS OBSERVATIONS

QSO	$z_{\text{em}}$	$\alpha$ (J2000)		$\delta$ (J2000)			Grating	Date	Time (s)	
H1146+111B .....	1.01	11	48	44.26	10	47	56.9	G190H	1996 Feb 21	12,500
H1146+111E .....	1.10	11	48	42.05	10	47	09.0	G190H	1996 Feb 20	10,180
H1146+111C .....	1.01	11	48	39.42	10	50	16.7	G190H	1996 Feb 27	12,450
H1146+111D .....	2.12	11	48	51.39	10	48	25.0	G190H	1996 Feb 24	7900
MC 1146+111.....	0.86	11	48	47.89	10	54	59.4	G190H	1995 Jul 26	5120

NOTE.—Units of right ascension are hours, minutes, and seconds, and units of declination are degrees, arcminutes, and arcseconds.

## 2. OBSERVATIONS

The *HST*-FOS observations of the five QSOs took place over the period 1995 July–1996 March; Table 1 contains the journal of observations. A ground-based image of the field with the QSOs marked is shown for reference in Figure 1.

The targets were acquired in binary mode into the 4"3 science aperture, followed by a peak-up into the 0"25  $\times$  2"0 slit, and the integrations proceeded with the G190H grating in place. The nominal wavelength coverage of the G190H grating is 1600–2300 Å; however, the signal-to-noise ratio (SNR) deteriorates rapidly below  $\approx$  1700 Å. A Lyman-limit system was apparently encountered along the line of sight toward the highest redshift member of the group, QSO D ( $z_{\text{em}} \approx 2.12$ ), and no significant flux was detected for this QSO. The estimated 0"03 centering error (FOS Handbook 1995) in the 4"3 aperture translates to  $\approx$  22 km s $^{-1}$  in the dispersion direction at 1900 Å. At the end of the exposure for each QSO, a PtCrNe arc spectrum was obtained to check the wavelength calibration independently. The data were reduced with the usual pipeline processing and standard calibration files. New wavelength coefficients for the four QSO spectra were calculated from the PtCrNe arc exposures using the STSDAS task "dispfity" in IRAF and used to recalibrate the standard pipeline dispersion solution, which was then applied to the spectra. The rms errors in the fits to obtain the wavelength coefficients were 0.03 Å, 0.02 Å, 0.02 Å, and 0.05 Å for QSOs A, B, C, and E, respectively.

The spectra of the four QSOs and their error arrays are presented in Figures 2, 3, 4, and 5. The individual exposure times were originally chosen to ensure approximately equal SNR for the spectra. The SNR per resolution element increases with wavelength, and in each spectrum the contin-

uum has SNR  $\approx$  20 at 1900 Å and  $\approx$  30 at 2300 Å. In Figure 5, deep absorption from the  $z_{\text{abs}} \approx z_{\text{em}}$  system in QSO E can be seen: N v  $\lambda\lambda$ 1238, 1242 at  $\approx$  2300 Å, Ly $\alpha$  at  $\approx$  2250 Å, O vi  $\lambda\lambda$ 1031, 1037 at  $\approx$  1915 Å, and Ly $\beta$  at  $\approx$  1900 Å. These ions are listed in Table 2.

## 3. ANALYSIS OF THE SPECTRA

### 3.1. Line Lists

The data were analyzed using the *HST* QSO Absorption Line Key Project software (JASON) as described in detail by Schneider et al. (1993). Briefly, each input spectrum (the emission lines and underlying continuum) was fitted with a spline "continuum" (see Figs. 2–5), and each spectrum and its error array were normalized by this fit to produce a flat spectrum in which the absorption lines were the only remaining features. A search was then performed using the instrumental profile to make an initial pass at detecting absorption lines. This initial search line list was the basis for a subsequent algorithm that fitted Gaussians to all of the detected absorption features, including those that were resolved. Resolved features were fitted with multiple instrumental profiles, and the Gaussian fits to these profiles were performed to minimize the  $\chi^2$  of the fit across the entire absorption feature. The final JASON output for each detected line includes the wavelength centroid ( $\lambda_{\text{obs}}$ ) and associated error ( $\sigma_{\lambda_{\text{obs}}}$ ); the measured equivalent width ( $W_{\text{obs}}$ ) and error ( $\sigma_{W_{\text{obs}}}$ ); the FWHM and error of the Gaussian fits; and the SNR of the line,  $\text{SNR} = |W_{\text{obs}}|/\sigma_{W_{\text{obs}}}$ . The significance level (SL) of the line was calculated as  $\text{SL} = |W_{\text{obs}}|/\bar{\sigma}_{W_{\text{obs}}}$ , where  $\bar{\sigma}_{W_{\text{obs}}}$  was the error in the measured equivalent width calculated from the error array interpolated across the absorption features. The SL also differs from the SNR in that  $\bar{\sigma}_{W_{\text{obs}}}$  is based on the measured line width, whereas  $\sigma_{W_{\text{obs}}}$  is based on the unresolved line profile. The difference between the SNR and SL will therefore be most apparent for (1) unresolved lines, where  $\bar{\sigma}_{W_{\text{obs}}} > \sigma_{W_{\text{obs}}}$  and (2) very broad lines in which  $\bar{\sigma}_{W_{\text{obs}}} < \sigma_{W_{\text{obs}}}$ . Expressions of the line significance in terms of  $\sigma$  throughout this paper refer to the SL calculated from the interpolated error array, unless otherwise noted. The 3.5  $\sigma$  and 5  $\sigma$  equivalent width limits are plotted for the four spectra in Figure 6. Tables 3, 4, 5, and 6 list the lines identified with  $\text{SL} > 3.5$  in QSOs A, B, C, and E, respectively. Each line list includes the centroid wavelength and associated error, the observed equivalent width and error, and the SL of the line.

### 3.2. Line Identifications

The criteria of the *HST* Key Project (CAT2) line search and finding algorithm were adopted to aid in identifying the lines, although the steps beyond the initial search for wave-

TABLE 2  
IONS IN THE  $z_{\text{abs}} \approx z_{\text{em}}$  SYSTEM OF QSO E  
(MC 1146+111)

$\lambda_{\text{obs}}$ (Å)	ID	Velocity (km s $^{-1}$ )
1900.4 .....	Ly $\beta$ 1025.7	2176
1907.4 .....	Ly $\beta$ 1025.7	130
1912.8 .....	O vi 1031.9	1900
1918.9 .....	O vi 1031.9	126
1923.5 .....	O vi 1036.3	1163
2253.7 .....	Ly $\alpha$ 1215.7	1850
2260.9 .....	Ly $\alpha$ 1215.7	61
2297.1 .....	N v 1238.8	1712
2303.6 .....	N v 1242.8	1933

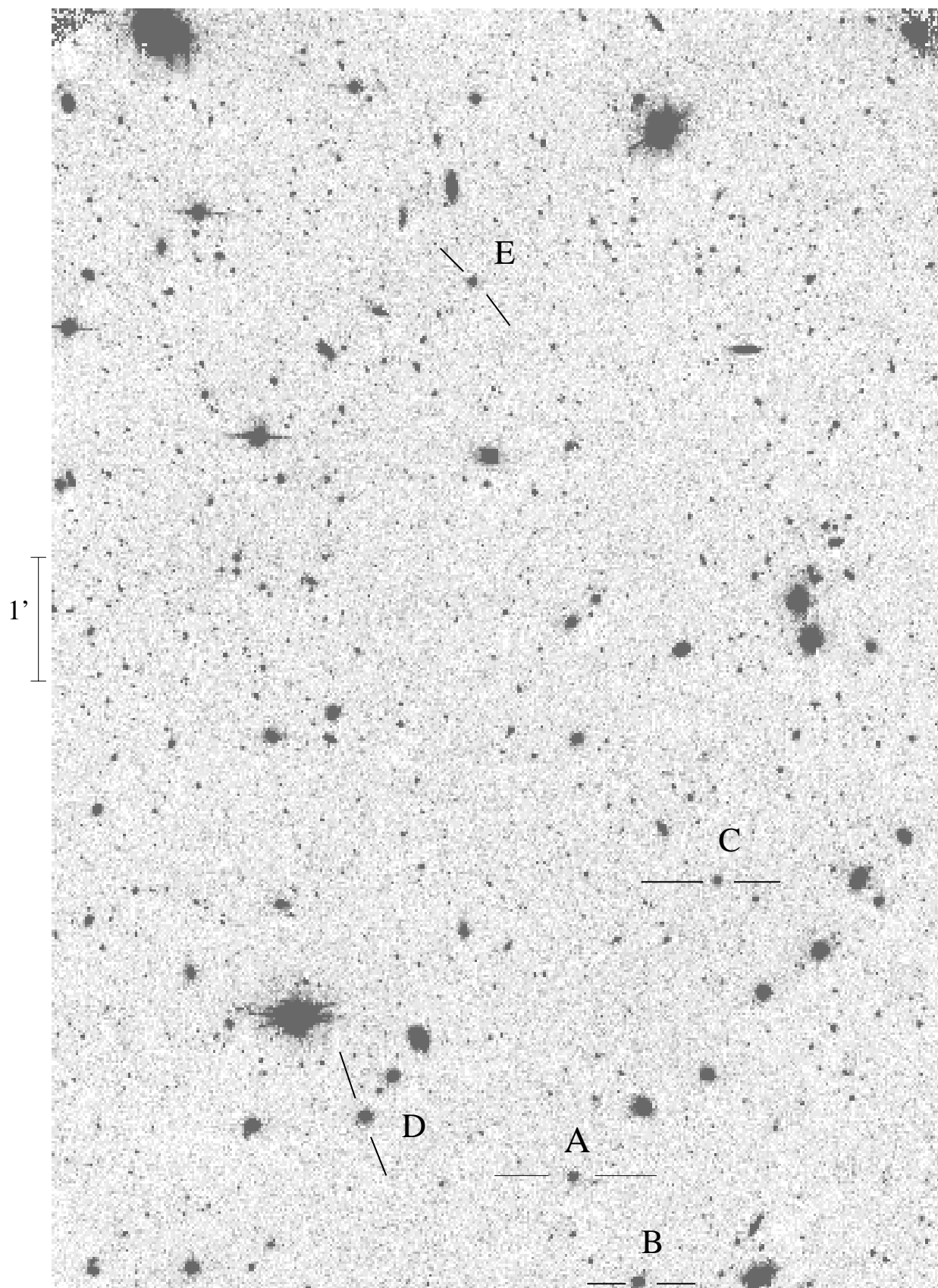


FIG. 1.—Ground-based *R* filter image obtained with the 4.2 m William Herschel Telescope by K. Lanzetta. The five QSOs observed with *HST*-FOS are labeled as by Hazard et al. (1979); no flux shortward of 2310 Å was present in the spectrum of QSO D. North is up, and east is to the left.

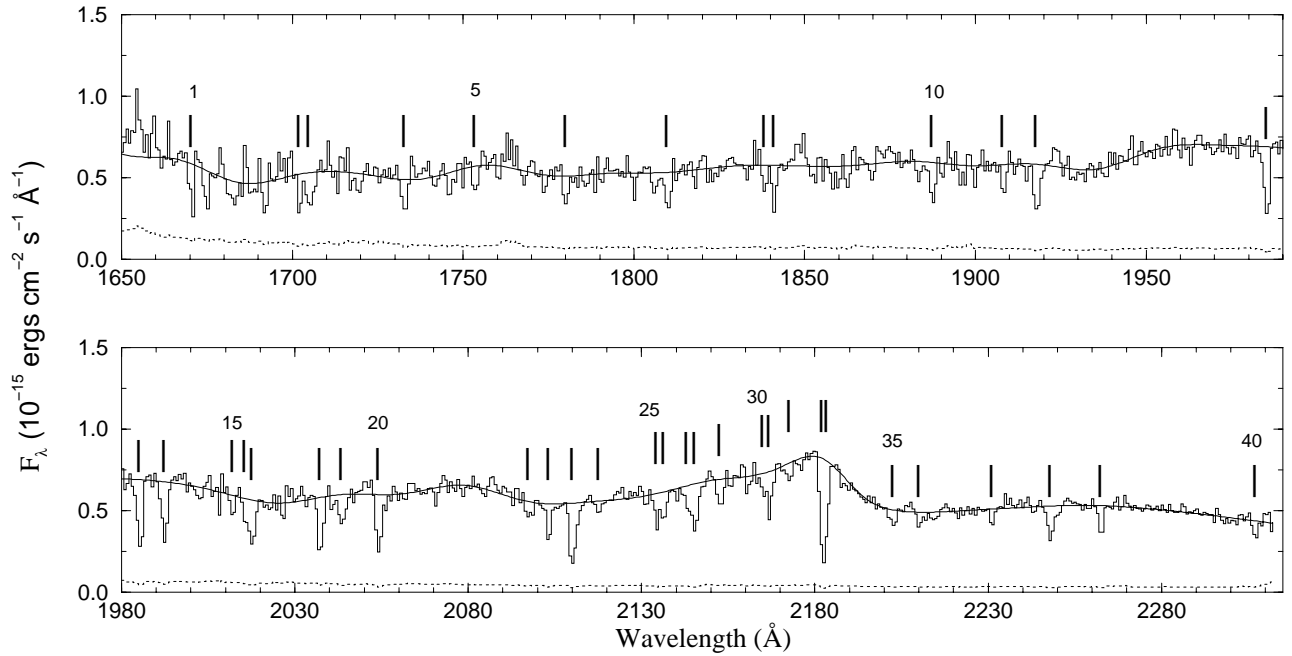


FIG. 2.—Unsmoothed, 4 pixel per resolution element *HST*-FOS G190H spectrum (resolution  $\lambda/\Delta\lambda \approx 1300$ ) of H1146+111B (QSO A). Absorption lines having significance level (SL) greater than 3.5 are marked. The dotted line is the  $1\sigma$  error in flux per pixel.

length agreement were performed manually. The procedure ensured that the line identifications were consistent with physical constraints. The lines searched for were the strongest expected one-electron, dipole transitions from the ground or excited fine-structure states for the most cosmologically abundant elements (see CAT2).

Candidate lines were searched for within  $1\text{ Å}$  or  $3\sigma_{\lambda_{\text{obs}}}$  of the expected wavelength, whichever was larger. The identification of any features as members of the H I Lyman series or as transitions due to the same ion of a metal line (i.e.,

either separate lines, such as C II  $\lambda 1036$  and C II  $\lambda 1334$ , or members of a doublet, e.g., C IV  $\lambda\lambda 1548, 1550$ ) required that the measured relative strengths of lines were consistent with the underlying physics and satisfied equations (3) and (4) of CAT2.

The process of identifying the absorption lines took four steps.

1. Ultraviolet transitions due to absorption in the interstellar medium of the Galaxy were identified using the list of

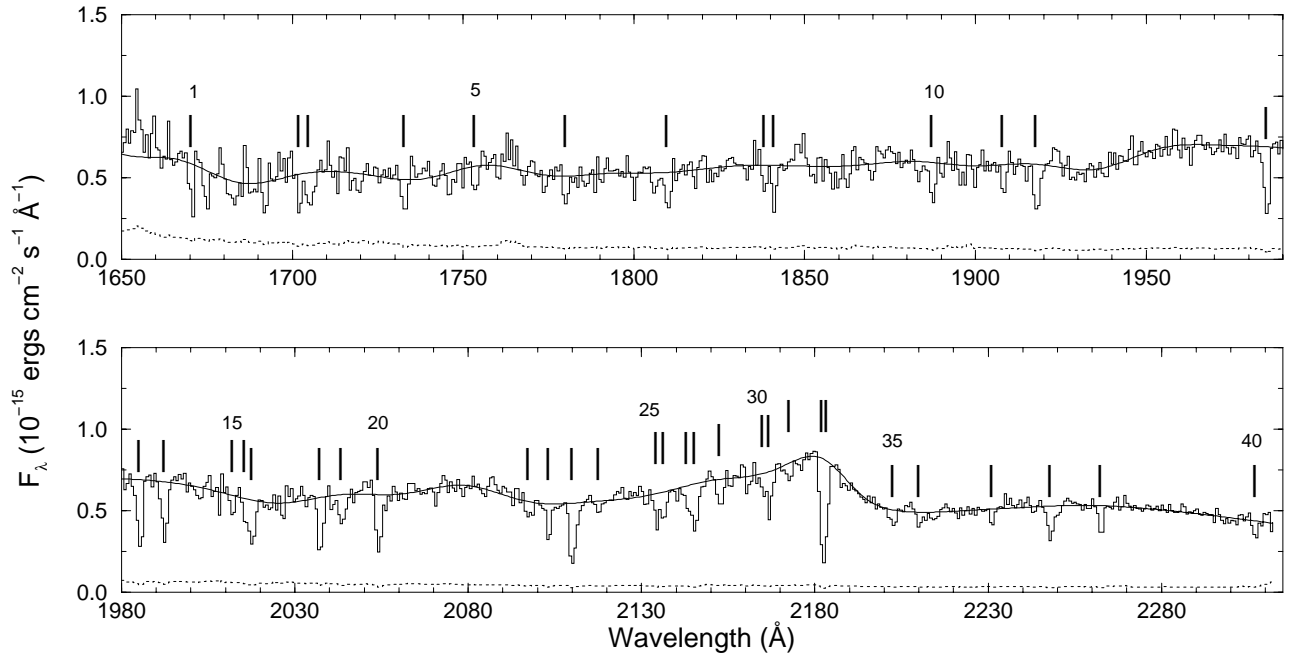


FIG. 3.—Unsmoothed, 4 pixel per resolution element *HST*-FOS G190H spectrum (resolution  $\lambda/\Delta\lambda \approx 1300$ ) of H1146+111E (QSO B). Absorption lines having SL greater than 3.5 are marked. The dotted line is the  $1\sigma$  error in flux per pixel.

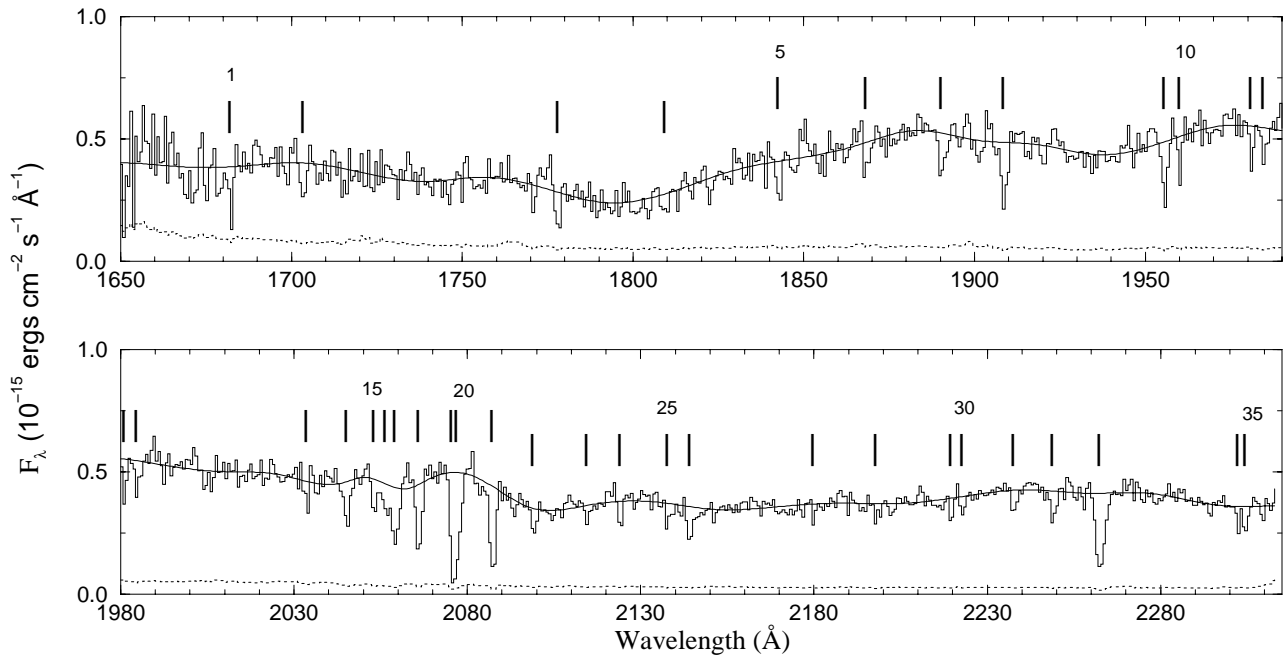


FIG. 4.—Unsmoothed, 4 pixel per resolution element *HST*-FOS G190H spectrum (resolution  $\lambda/\Delta\lambda \approx 1300$ ) of H1146+111C (QSO C). Absorption lines having SL greater than 3.5 are marked. The dotted line is the  $1\sigma$  error in flux per pixel.

Savage et al. (1993). The wavelength interval covered by the data is fairly bereft of interstellar lines, and only Al II  $\lambda 1670$  was detected.

2. Next, it was assumed that all of the detected lines were due to Ly $\alpha$ , and a search was performed for higher order Lyman lines and associated metal lines using the wavelengths and oscillator strengths of Verner, Barthel, & Tytler (1994).

3. Since the spectra of QSOs A, B, and C do not extend to the Ly $\alpha$  emission line, the finite wavelength coverage

meant that there were small regions in which Ly $\beta$  absorption could appear without the corresponding Ly $\alpha$  absorption line being visible ( $\approx 1950$ – $2062$  Å in A and C and  $\approx 1950$ – $2154$  Å in B). The absorption lines not identified as Ly $\alpha$  or metal lines in these regions initially were assumed at this point to be possible Ly $\beta$  lines, and a search was again undertaken for higher order Lyman lines and metal lines associated with these potential systems.

4. In regions where the corresponding Ly $\alpha$  or Ly $\beta$  line was not accessible to allow identification in the previous

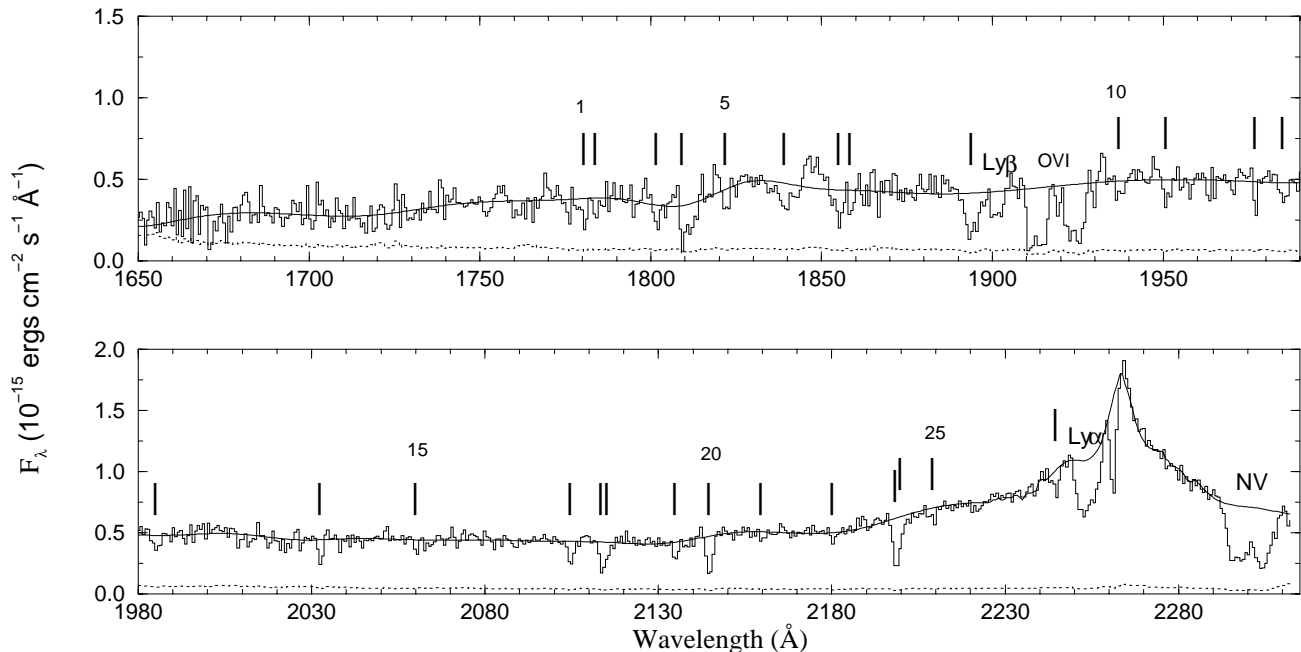


FIG. 5.—Unsmoothed, 4 pixel per resolution element *HST*-FOS G190H spectrum (resolution  $\lambda/\Delta\lambda \approx 1300$ ) of MC 1146+111 (QSO E). Absorption lines having SL greater than 3.5 are marked. The dotted line is the  $1\sigma$  error in flux per pixel.

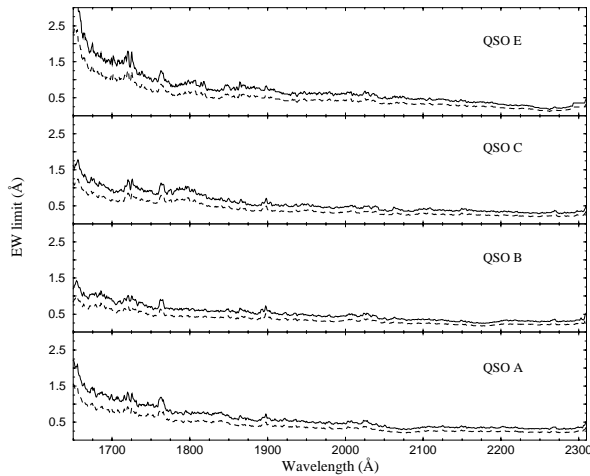


FIG. 6.—Observed equivalent width limits for 5  $\sigma$  (solid line) and 3.5  $\sigma$  (dashed line) detection thresholds in the four QSO spectra.

step, a search was performed among the remaining detected lines for the strongest doublets that may be seen at  $z < 0.9$ , including C IV  $\lambda\lambda 1548, 1550$ , Si IV  $\lambda\lambda 1393, 1402$ , Al IV  $\lambda\lambda 1854, 1862$  and O VI  $\lambda\lambda 1031, 1037$ . In the case of these doublets, the identification was accepted provided the members of the components satisfied equations (3) and (4) of CAT2. The remaining lines throughout the four spectra that were not identified during the course of the previous steps were then taken as being due to Ly $\alpha$  absorption. The line identifications are listed in the last column of Tables 3–6.

### 3.3. Comments on Individual QSO Spectra

#### 3.3.1. QSO A ( $z_{\text{em}} = 1.01$ )

The line of sight toward QSO A contains 40 absorption lines with SL  $> 3.5$ . The strongest line is a blend with components identified by JASON at 2035.1 Å and 2036.7 Å,

TABLE 3  
ABSORPTION-LINE LIST FOR QSO A (H1146 + 111B)

Line Number	$\lambda_{\text{obs}}$ (Å)	$\sigma_{\lambda_{\text{obs}}}$ (Å)	$W_{\text{obs}}$ (Å)	$\sigma_{W_{\text{obs}}}$ (Å)	SL	$z_{\text{abs}}$	ID
1 .....	1670.15	0.20	2.38	0.39	8.84	0.0000	Al II 1670.8
2 .....	1679.59	0.30	1.06	0.34	4.40	0.3816	H I 1215.7
3 .....	1718.13	0.29	1.75	0.39	7.73	0.6750	Ly $\beta$ 1025.7
4 .....	1772.46	0.22	0.65	0.15	4.12	0.7280	Ly $\beta$ 1025.7
5 .....	1778.15	0.14	1.53	0.20	10.47	0.4627	H I 1215.7
6 .....	1801.61	0.21	0.62	0.14	4.26	0.4820	H I 1215.7
7 .....	1855.26	0.14	1.41	0.18	11.23	0.5261	H I 1215.7
8 .....	1859.78	0.11	2.41	0.19	18.90	0.5298	H I 1215.7
9 .....	1868.51	0.21	0.78	0.17	6.42	0.9674	Ly $\delta$ 949.7
10 .....	1882.96	0.20	0.84	0.16	7.82	0.8357	Ly $\beta$ 1025.7 <sup>a</sup>
11 .....	1887.66	0.14	0.65	0.10	6.14	0.5528	H I 1215.7
12 .....	1906.96	0.23	0.65	0.15	5.83	1.0078	Ly $\delta$ 949.7
13 .....	1913.38	0.10	0.95	0.09	8.95	0.9674	Ly $\gamma$ 972.5
14 .....	1918.79	0.17	0.58	0.10	5.42	0.5784	H I 1215.7
15 .....	1952.72	0.11	0.82	0.12	8.40	1.0079	Ly $\gamma$ 972.5
16 .....	2011.45	0.15	0.61	0.12	6.32	0.6546	H I 1215.7
17 .....	2018.56	0.15	1.53	0.15	16.14	0.9679	Ly $\beta$ 1025.7
18 .....	2029.98	0.12	0.76	0.09	7.65	0.6698	H I 1215.7
19 .....	2035.12	0.16	0.83	0.23	9.36	0.6741	H I 1215.7
20 .....	2036.73	0.13	1.90	0.28	21.41	0.6754	H I 1215.7
21 .....	2054.16	0.11	0.75	0.09	11.56	0.3268	C IV 1548.2
22 .....	2057.85	0.14	0.49	0.07	7.46	0.3270	C IV 1550.8
23 .....	2059.56	0.10	1.02	0.08	15.31	1.0079	Ly $\beta$ 1025.7
24 .....	2061.33	0.09	0.97	0.12	14.64	0.6956	H I 1215.7
25 .....	2072.20	0.15	0.42	0.08	7.09	1.0081	O VI 1031.9
26 .....	2083.75	0.13	0.43	0.06	7.21	1.0082	O VI 1037.6
27 .....	2095.28	0.18	0.34	0.08	5.13	0.7236	H I 1215.7
28 .....	2100.94	0.08	0.83	0.06	11.30	0.7282	H I 1215.7
29 .....	2110.80	0.09	0.72	0.08	9.76	0.6747	Si II 1260.4
30 .....	2117.26	0.31	0.53	0.12	7.47	0.7416	H I 1215.7
31 .....	2135.24	0.33	0.36	0.11	5.09	0.7564	H I 1215.7
32 .....	2162.48	0.09	0.72	0.06	10.50	0.7788	H I 1215.7
33 .....	2167.23	0.07	0.89	0.06	13.39	0.7827	H I 1215.7
34 .....	2180.96	0.25	0.24	0.07	3.62	0.7940	H I 1215.7 <sup>b</sup>
35 .....	2193.86	0.06	0.94	0.08	13.79	0.8046	H I 1215.7
36 .....	2211.86	0.13	0.47	0.06	6.88	0.8195	H I 1215.7
37 .....	2231.48	0.11	0.84	0.09	13.46	0.8356	H I 1215.7
38 .....	2261.45	0.36	0.34	0.10	5.53	0.8602	H I 1215.7
39 .....	2302.25	0.11	0.76	0.09	10.62	0.8938	H I 1215.7
40 .....	2306.88	0.12	0.82	0.10	9.96	0.8976	H I 1215.7

<sup>a</sup> Blend with Ly $\epsilon$   $\lambda$ 937.8 at  $z_{\text{abs}} = 1.0078$ .

<sup>b</sup> Possible blend with O I  $\lambda$ 1302.2 at  $z_{\text{abs}} = 0.6748$ .

TABLE 4  
ABSORPTION-LINE LIST FOR QSO B (H1146+111E)

Line Number	$\lambda_{\text{obs}}$ (Å)	$\sigma_{\lambda_{\text{obs}}}$ (Å)	$W_{\text{obs}}$ (Å)	$\sigma_{W_{\text{obs}}}$ (Å)	SL	$z_{\text{abs}}$	ID
1 .....	1670.24	0.23	0.75	0.18	3.88	0.0000	Al II 1670.8
2 .....	1701.64	0.21	0.72	0.15	4.18	0.6590	Ly $\beta$ 1025.7
3 .....	1704.59	0.25	1.12	0.25	7.38	0.7948	Ly $\delta$ 949.7
4 .....	1732.58	0.22	0.77	0.20	5.20	0.6891	Ly $\beta$ 1025.7
5 .....	1753.10	0.23	0.50	0.12	4.02	0.7943	C III 977.0
6 .....	1779.73	0.20	0.56	0.12	4.65	0.7351	Ly $\beta$ 1025.7
7 .....	1809.53	0.15	0.83	0.15	6.83	0.7642	Ly $\beta$ 1025.7
8 .....	1838.02	0.23	0.45	0.11	4.04	0.5119	H I 1215.7
9 .....	1840.80	0.14	0.74	0.11	6.29	0.7946	Ly $\beta$ 1025.7
10 .....	1887.12	0.14	0.79	0.13	7.93	0.5523	H I 1215.7
11 .....	1907.81	0.19	0.50	0.10	4.80	0.5693	H I 1215.7
12 .....	1917.63	0.10	1.05	0.12	10.74	0.5774	H I 1215.7
13 .....	1984.96	0.07	1.25	0.10	14.97	0.6328	H I 1215.7
14 .....	1992.11	0.08	1.12	0.10	12.84	0.6387	H I 1215.7
15 .....	2011.81	0.22	0.38	0.09	3.99	0.6549	H I 1215.7
16 .....	2015.34	0.23	0.44	0.10	5.06	0.7954	Fe III 1122.5
17 .....	2017.38	0.11	0.96	0.14	11.13	0.6595	H I 1215.7
18 .....	2037.02	0.07	1.09	0.10	11.80	0.6756	H I 1215.7
19 .....	2043.17	0.17	0.75	0.11	10.23	0.6807	H I 1215.7
20 .....	2053.87	0.05	1.13	0.08	16.54	0.6895	H I 1215.7
21 .....	2097.18	0.23	0.37	0.09	5.39	0.7251	H I 1215.7
22 .....	2102.95	0.09	0.70	0.06	10.03	0.7299	H I 1215.7
23 .....	2109.79	0.06	1.67	0.09	24.78	0.7355	H I 1215.7
24 .....	2117.29	0.25	0.23	0.06	3.61	0.7417	H I 1215.7
25 .....	2134.10	0.12	0.55	0.06	9.14	0.7555	H I 1215.7
26 .....	2136.18	0.13	0.46	0.08	7.70	0.7572	H I 1215.7 <sup>a</sup>
27 .....	2142.91	0.45	0.41	0.22	7.06	0.7958	Si II 1193.3
28 .....	2145.06	0.20	0.90	0.21	15.53	0.7645	H I 1215.7
29 .....	2152.35	0.12	0.47	0.07	7.91	0.7705	H I 1215.7
30 .....	2164.73	0.19	0.27	0.05	5.24	0.7942	Si II 1206.5
31 .....	2166.60	0.08	0.61	0.05	12.00	0.7822	H I 1215.7
32 .....	2172.37	0.19	0.24	0.05	4.85	0.7870	H I 1215.7
33 .....	2181.89	0.11	1.28	0.21	25.79	0.7948	H I 1215.7
34 .....	2183.14	0.19	0.62	0.18	12.53	0.7958	H I 1215.7
35 .....	2202.23	0.20	0.39	0.09	6.04	0.8115	H I 1215.7
36 .....	2209.88	0.23	0.25	0.06	4.04	0.8178	H I 1215.7
37 .....	2230.82	0.17	0.34	0.06	5.50	0.8351	H I 1215.7
38 .....	2247.63	0.07	0.74	0.07	12.85	0.8489	H I 1215.7
39 .....	2262.23	0.10	0.56	0.05	9.59	0.7948	Si II 1260.4
40 .....	2306.78	0.17	0.39	0.07	5.50	0.8975	H I 1215.7

<sup>a</sup> Probable blend with Si II  $\lambda$ 1190.4 at  $z_{\text{abs}} = 0.7941$ .

corresponding to a separation of  $\approx 240 \text{ km s}^{-1}$ . Given the strength of this complex, the line at  $2110.8 \text{ Å}$  has been classified as Si II  $\lambda$ 1260. Although no other Si II transitions were identified, they are all expected to be weaker, and within the measurement errors the constraints of equations (3) and (4) of CAT2 were satisfied. No other metal lines were identified in this system. Two systems were identified by lines other than Ly $\alpha$ . The first, a heavy-element system at  $z_{\text{abs}} = 1.0080$ , lies within  $\approx 600 \text{ km s}^{-1}$  of the emission redshift of the QSO and exhibits absorption due to Ly $\beta$ , Ly $\gamma$ , Ly $\delta$ , and possibly Ly $\epsilon$  (blended with Ly $\beta$  at  $z_{\text{abs}} = 0.8357$ ), as well as the high-ionization species O VI  $\lambda$ 1032, 1037. The second, at  $z_{\text{abs}} = 0.9676$ , contains Ly $\beta$ , Ly $\gamma$ , and Ly $\delta$ . This system was accepted because of the wavelength agreement and because it satisfied equation (3) of CAT2. However, the Ly $\beta$  line identified at  $2018.6 \text{ Å}$  is much wider than that of the Ly $\gamma$  or Ly $\delta$  lines. Although JASON fitted the  $2018.6 \text{ Å}$  feature with a single line, the FWHM of the Gaussian is  $\approx 3.0 \text{ Å}$ , large enough that it likely is a blend of two or more

lines. If one of them is Ly $\alpha$ , it is potentially a coincidence (as defined below) with the Ly $\alpha$  line at  $2017.4 \text{ Å}$  in QSO B, depending on the exact centers of the lines comprising the blend. We note that the velocity difference between the measured  $2018.6 \text{ Å}$  line in QSO A and the  $2017.4 \text{ Å}$  line in QSO B is greater than  $150 \text{ km s}^{-1}$  and would not qualify as a coincidence. Finally, a C IV system was found at  $z_{\text{abs}} = 0.3269$ .

### 3.3.2. QSO B ( $z_{\text{em}} = 1.10$ )

Forty absorption lines having  $\text{SL} > 3.5$  were identified toward QSO B. JASON deconvolved the strong Ly $\alpha$  feature at  $\approx 2182 \text{ Å}$  into two separate lines at  $2181.9 \text{ Å}$  and  $2183.1 \text{ Å}$ , corresponding to a velocity separation of  $165 \text{ km s}^{-1}$ . These lines appear separately in Table 4, but since this value is less than the  $230 \text{ km s}^{-1}$  resolution of the FOS, the two lines were combined into one with  $z_{\text{abs}} = 0.7953$  for the purposes of the later analysis. Other absorption lines identified in this system were Ly $\beta$ , Ly $\delta$ , C III  $\lambda$ 977, Fe III  $\lambda$ 1122, Si



TABLE 5  
ABSORPTION-LINE LIST FOR QSO C (H1146+111C)

Line Number	$\lambda_{\text{obs}}$ (Å)	$\sigma_{\lambda_{\text{obs}}}$ (Å)	$W_{\text{obs}}$ (Å)	$\sigma_{W_{\text{obs}}}$ (Å)	SL	$z_{\text{abs}}$	ID
1 .....	1681.91	0.22	0.89	0.20	4.23	0.3835	H I 1215.7
2 .....	1703.22	0.31	0.73	0.24	4.18	0.4011	H I 1215.7
3 .....	1777.74	0.15	0.96	0.15	5.89	0.4624	H I 1215.7
4 .....	1809.09	0.63	0.63	0.23	3.81	0.7637	Ly $\beta$ 1025.7 <sup>a</sup>
5 .....	1842.36	0.17	0.70	0.12	5.38	0.5155	H I 1215.7
6 .....	1867.96	0.21	0.52	0.15	4.27	0.5366	H I 1215.7
7 .....	1890.02	0.18	0.79	0.14	7.41	0.5547	H I 1215.7
8 .....	1908.29	0.10	1.07	0.13	10.28	0.8604	Ly $\beta$ 1025.7
9 .....	1955.38	0.10	0.90	0.08	9.14	0.6085	H I 1215.7
10 .....	1959.75	0.19	0.46	0.09	4.69	0.6121	H I 1215.7
11 .....	1980.78	0.17	0.48	0.09	5.29	0.2794	C IV 1548.2
12 .....	1984.35	0.18	0.42	0.08	4.82	0.2796	C IV 1550.8
13 .....	2033.43	0.23	0.33	0.08	3.94	0.6727	H I 1215.7
14 .....	2045.03	0.12	0.76	0.10	9.84	0.6822	H I 1215.7
15 .....	2052.89	0.13	0.52	0.07	7.15	1.0014	Ly $\beta$ 1025.7
16 .....	2056.18	0.30	0.62	0.19	8.43	0.3259	H I 1215.7
17 .....	2058.93	0.14	1.21	0.18	16.37	0.6937	H I 1215.7
18 .....	2065.68	0.06	1.11	0.09	12.99	1.0018	O VI 1031.9
19 .....	2075.16	0.09	1.05	0.24	14.80	1.0110	O VI 1037.6 <sup>b</sup>
20 .....	2076.64	0.17	1.79	0.29	25.20	1.0014	O VI 1031.9
21 .....	2087.00	0.04	1.76	0.09	24.99	1.0113	O VI 1037.6
22 .....	2098.80	0.14	0.53	0.10	6.58	0.7265	H I 1215.7
23 .....	2114.27	0.25	0.28	0.07	3.71	0.7392	H I 1215.7
24 .....	2123.92	0.16	0.44	0.07	5.70	0.7471	H I 1215.7
25 .....	2137.63	0.24	0.52	0.11	7.30	0.7584	H I 1215.7
26 .....	2143.94	0.09	0.78	0.09	10.53	0.7636	H I 1215.7
27 .....	2179.63	0.24	0.27	0.07	3.78	0.7929	H I 1215.7
28 .....	2197.77	0.23	0.35	0.09	5.35	0.8079	H I 1215.7
29 .....	2219.24	0.15	0.40	0.06	5.80	0.8255	H I 1215.7
30 .....	2222.53	0.19	0.29	0.06	4.67	0.8282	H I 1215.7
31 .....	2237.43	0.15	0.36	0.06	6.08	0.8405	H I 1215.7
32 .....	2248.61	0.11	0.57	0.07	9.76	0.8497	H I 1215.7
33 .....	2262.22	0.05	2.38	0.09	37.47	0.8609	H I 1215.7
34 .....	2302.15	0.16	0.39	0.06	5.57	0.8937	H I 1215.7
35 .....	2304.26	0.15	0.44	0.07	6.18	0.8955	H I 1215.7

<sup>a</sup> Blend with Ly $\gamma$  972.5 at  $z_{\text{abs}} = 0.8602$ , C II 904 at  $z_{\text{abs}} = 1.0014$ .

<sup>b</sup> Possible blend with C II 1036.3 in  $z_{\text{abs}} = 1.0014$  system.

III  $\lambda$ 1206, and Si II  $\lambda$ 1260. The Si II  $\lambda\lambda$ 1190, 1193 doublet also appears to be present, although the weaker  $\lambda$ 1190 component is blended with a Ly $\alpha$  line.

### 3.3.3. QSO C ( $z_{\text{em}} = 1.01$ )

The most interesting features of the QSO C spectrum are two strong lines at  $\approx 2076$  Å and  $\approx 2087$  Å, which we have identified as a O VI  $\lambda\lambda$ 1032, 1037 system at  $z_{\text{abs}} = 1.0110$ , the approximate redshift of the QSO itself. The velocity separation between this doublet and the similar one seen in the spectrum of QSO A described above is  $\approx 900$  km s<sup>-1</sup>, suggesting that these QSOs are members of the same cluster, and that the O VI absorption arises in the cluster itself. In addition, the  $\lambda$ 1032 component of this doublet appears to be blended with O VI  $\lambda$ 1037 (and possibly C II  $\lambda$ 1036) in a second system at  $z_{\text{abs}} = 1.0018$ ,  $\approx 2800$  km s<sup>-1</sup> away from the first system. Also seen in this system are lines due to O VI  $\lambda$ 1032, Ly $\beta$ , and possibly C II  $\lambda$ 903 blended with Ly $\beta$  at  $z_{\text{abs}} = 0.7637$ . This second system is separated from the one identified in QSO A by  $\approx 1800$  km s<sup>-1</sup>. The blending of the lines in this region makes unequivocal identifications in this region difficult, but the possible scenarios would all satisfy equations (3) and (4) of CAT2. The spectrum contains a total of 35 absorption lines with SL > 3.5.

### 3.3.4. QSO E ( $z_{\text{em}} = 0.86$ )

The spectrum of QSO E contains no detected metal lines beyond the  $z_{\text{abs}} \approx z_{\text{em}}$  system, although several Ly $\alpha$ –Ly $\beta$  pairs were identified. The two lines at 2198.1 Å and 2199.6 Å are separated by less than 230 km s<sup>-1</sup> and were merged into one Ly $\alpha$  line for the later analysis. A total of 26 absorption lines possessing SL > 3.5 were found up to  $z_{\text{abs}} \approx 0.85$ , greater than 3000 km s<sup>-1</sup> from the emission redshift.

### 3.4. The Ly $\alpha$ Lines

The comprehensive list of 100 identified Ly $\alpha$  lines having SL > 3.5 includes 80 lines with SL > 4.5, of which 65 lines occur in the spectra of QSOs A, B, and C in the interval  $0.44 < z < 0.90$  (22 in A, 23 in B, and 20 in C). The remaining 15 lines from QSO E occur in the interval  $0.44 < z < 0.85$ , greater than 3000 km s<sup>-1</sup> from the emission redshift. Eliminating the portions of the spectrum of QSO E that are not useful because of the  $z_{\text{abs}} \approx z_{\text{em}}$  system, the total redshift interval is  $\Delta z = 1.7621$  with a mean redshift of  $\bar{z} = 0.6644$ . There are 66 Ly $\alpha$  lines having rest equivalent width  $W_0 > 0.24$  Å and SL > 4.5. The number of lines per unit redshift for *uncorrelated* lines is  $dN/dz = 36.7 \pm 4.6 = (dN/dz)_0(1 + \bar{z})^{\gamma}$ . The most recent results from the

TABLE 6  
ABSORPTION-LINE LIST FOR QSO E (MC 1146+111)

Line Number	$\lambda_{\text{obs}}$ (Å)	$\sigma_{\lambda_{\text{obs}}}$ (Å)	$W_{\text{obs}}$ (Å)	$\sigma_{W_{\text{obs}}}$ (Å)	SL	$z_{\text{abs}}$	ID
1 .....	1780.30	0.18	0.86	0.20	5.26	0.4645	H I 1215.7
2 .....	1783.68	0.28	0.56	0.21	3.45	0.7390	Ly $\beta$ 1025.7
3 .....	1801.50	0.27	0.76	0.23	4.05	0.7563	Ly $\beta$ 1025.7
4 .....	1808.90	0.15	1.19	0.23	7.09	0.7635	Ly $\beta$ 1025.7
5 .....	1821.82	0.29	0.60	0.20	4.20	0.4986	H I 1215.7
6 .....	1838.90	0.54	1.80	0.34	12.71	0.5127	H I 1215.7
7 .....	1854.97	0.17	1.08	0.19	7.05	0.8085	Ly $\beta$ 1025.7
8 .....	1858.24	0.19	0.66	0.13	4.63	0.5286	H I 1215.7
9 .....	1893.66	0.20	2.84	0.29	20.05	0.5577	H I 1215.7
10 .....	1936.98	0.42	0.50	0.18	4.44	0.5933	H I 1215.7
11 .....	1950.63	0.23	0.63	0.16	5.30	0.6046	H I 1215.7
12 .....	1976.74	0.21	0.53	0.11	4.37	0.6260	H I 1215.7
13 .....	1984.86	0.25	0.63	0.16	5.56	0.6327	H I 1215.7
14 .....	2032.19	0.13	0.74	0.10	6.80	0.6717	H I 1215.7
15 .....	2059.88	0.25	0.36	0.09	3.62	0.6944	H I 1215.7
16 .....	2104.42	0.09	0.84	0.10	9.84	0.7311	H I 1215.7
17 .....	2113.35	0.08	0.98	0.07	11.14	0.7384	H I 1215.7
18 .....	2115.04	0.17	0.52	0.09	5.89	0.7398	H I 1215.7
19 .....	2134.68	0.12	0.60	0.10	7.32	0.7560	H I 1215.7
20 .....	2144.43	0.06	1.49	0.09	18.64	0.7640	H I 1215.7
21 .....	2159.58	0.26	0.26	0.07	3.49	0.7765	H I 1215.7
22 .....	2180.04	0.26	0.25	0.07	3.48	0.7933	H I 1215.7
23 .....	2198.19	0.08	1.03	0.59	15.96	0.8082	H I 1215.7
24 .....	2199.62	1.25	0.80	0.64	12.44	0.8094	H I 1215.7
25 .....	2208.93	0.29	0.35	0.09	5.99	0.8170	H I 1215.7
26 .....	2244.46	0.13	0.33	0.05	7.01	0.8463	H I 1215.7

*HST* Key Project give  $(dN/dz)_0 = 32.7 \pm 4.2$  and  $\gamma = 0.26 \pm 0.22$  (Weymann et al. 1998), so that one would expect to find  $37.4 \pm 4.8$  Ly $\alpha$  lines having  $SL > 4.5$  and  $W_0 > 0.24$  Å. Thus, our observed number of Ly $\alpha$  lines is within 1  $\sigma$  of the expected value if the lines are uncorrelated.<sup>4</sup>

#### 4. VELOCITY CROSS-CORRELATIONS

The final line lists represent four distinct probes of structure in the universe at intermediate redshifts, probes that may not be independent of each other since the lines of sight have relatively small physical separations. The first question to be addressed is whether two lines can be found close to the same wavelength in two different spectra, and how often such pairs occur compared with a random distribution of lines. A nonrandom occurrence of lines paired in wavelength along distinct lines of sight may be interpreted as evidence that the absorbers, whether as individual large structures or as a clustered association of smaller ones, span those lines of sight. If such pairs exist, subsequent comparison of the equivalent widths of the member lines can be used to describe the uniformity of absorption across the scales involved. These two pieces of information in principle place constraints on the absorber sizes and shapes if correlations exist. Since the strength of correlations may be affected by the strengths of the lines involved (i.e., weak lines paired with other weak lines, weak with strong, etc.), we formed several samples of increasingly stronger lines. As noted above, in instances when two Ly $\alpha$  lines were identi-

fied at a separation of less than  $230 \text{ km s}^{-1}$  in an individual spectrum, a single line was formed having a redshift equal to the average of the two redshifts and an equivalent width summed from the individual equivalent widths.

##### 4.1. Sample Definitions

The Ly $\alpha$  lines detected in the four spectra with  $SL > 3.5$  and  $\lambda > 1750$  Å were assembled in Sample 1. Although the possibility exists that some of these weaker lines are spurious, more conservative approaches may miss real correlations that appear or are strengthened by their inclusion. The 16 lines in Sample 1 with  $3.5 < SL < 4.5$  have  $\langle W_0 \rangle = 0.23 \pm 0.10$  Å. Sample 2 included all of the lines identified as Ly $\alpha$  with  $SL > 4.5$ , but no equivalent width threshold was imposed; the increasing SNR across the spectra meant that lines were measurable down to progressively smaller equivalent widths, so that imposing such a cutoff may have unnecessarily limited the sample size, possibly making correlations arising from the presence of weaker lines more difficult to detect. For Sample 3, limits of  $SL > 5.0$  and  $W_0 > 0.24$  Å were imposed, leaving a total of 63 lines. Samples 4 and 5 also contained the greater than  $5 \sigma$  lines, and the  $W_0$  cutoff was increased to 0.32 and 0.40 Å, respectively. Table 7 summarizes the number of lines detected along the four lines of sight for each of the five samples, as well as the calculated  $dN/dz$  for the sample.

All of the samples included the strong Ly $\alpha$  lines arising in systems in which there were also identified metal lines. While these systems may have intrinsically different cross sections than absorbers without detected heavy-element absorption, it is unknown if the systems responsible for weak and strong lines are related. Observations of gravitational lenses along multiple lines of sight have demon-

<sup>4</sup> The error on  $dN/dz$  will be larger if the sample contains correlated lines, but this effect will be small for the numbers discussed; for example,  $\approx 3\%$  larger if six lines are in common between A and B.

TABLE 7  
CRITERIA FOR THE  $\text{Ly}\alpha$  LINE SAMPLES

SAMPLE	SL LIMIT	$W_0$ CUTOFF ( $\text{\AA}$ )	NUMBER OF LINES				$dN/dz$
			A	B	C	E	
1 .....	3.5	...	24	27	24	21	$54.5 \pm 5.6$
2 .....	4.5	...	22	23	20	15	$45.4 \pm 5.1$
3 .....	5.0	0.24	20	18	13	12	$35.8 \pm 4.4$
4 .....	5.0	0.32	17	14	9	11	$28.9 \pm 3.9$
5 .....	5.0	0.40	15	12	8	8	$25.7 \pm 3.6$

strated large variations in column density even over kiloparsec scales in metal-line systems with strong  $\text{Ly}\alpha$  lines (Smette et al. 1995; Monier et al. 1998). If similar absorbers span any two of the sightlines here, they could exhibit such variations, or two lines may arise in distinct absorbers that are nonetheless contained in a larger structure. In the end, the distinction may not be relevant for our moderate-resolution data, given that metal-line absorption has been found to be associated with  $\text{Ly}\alpha$  lines down to column densities of  $N(\text{H I}) \approx 10^{12} \text{ atoms cm}^{-2}$  (Cowie et al. 1995). One can be sure that most, if not all, of the lines identified here as  $\text{Ly}\alpha$  have associated metal lines that would be detectable with higher resolution and SNR.

#### 4.2. Calculation of Cross-Correlations

Here we consider the correlation of absorption lines in velocity space between the lines of sight in the six pairs for the five samples. The nonrelativistic velocity difference,  $\Delta v$ , as measured by an observer at the absorption systems was calculated between all identified  $\text{Ly}\alpha$  lines for the six combinations (A/B, A/C, B/C, etc.) as

$$\Delta v = c \frac{\Delta z}{1 + \bar{z}}, \quad (1)$$

where  $\Delta z = |z_1 - z_2|$  and  $\bar{z} = (z_1 + z_2)/2$ , and  $z_1$  and  $z_2$  are the redshifts of the  $\text{Ly}\alpha$  lines along different lines of sight. The resulting velocity differences were binned in  $150 \text{ km s}^{-1}$  intervals, a value determined by D97 as the FWHM of a Gaussian fit to the distribution of nearest neighbor velocities using *HST*-FOS G190H spectra of Q0107–025A,B, a QSO pair similar to QSOs A and B.

Figure 7 shows the velocity cross-correlations of Samples 1 and 2 out to  $5000 \text{ km s}^{-1}$  for each of the six QSO combinations, in order of increasing spatial separation of the QSO pairs—from  $\approx 220 h^{-1} \text{ kpc}$  in the A/B pair in the upper left-hand corner to  $\approx 1.8 h^{-1} \text{ Mpc}$  in the widest separation pair (B/E) in the lower right-hand corner. The dashed lines in the panels represent the random expectations for pairs of lines in the various bins that would occur between uncorrelated lines of sight and were calculated from Monte Carlo simulations as described below.

##### 4.2.1. Monte Carlo Simulations

Individual spectra were simulated in which the probability of finding a line at any given redshift took the functional form

$$p(z) \approx A(1 + z)^\gamma, \quad (2)$$

where  $A$  is a normalization constant chosen so that  $\int_0^1 p(z) dz = 1$  and  $\gamma$  describes the redshift evolution of the number of lines. The simulations were performed for

$\gamma = 0.26$ , as found by the *HST* Key Project over the interval  $0 < z < 1.6$  (Weymann et al. 1998). The simulation generated  $N$  lines, where  $N$  was taken from the Poisson distribution around the expected value of  $dN/dz$  calculated from the observations along the four lines of sight (see Table 7). The velocity cross-correlations between pairs of simulated spectra were then performed in the same way as for the actual data as described above. One thousand simulations were used to establish the random levels for each sample. The Monte Carlo expectations are overplotted as dashed lines on the panels of Figure 7 and are the same for the six QSO pairs in a given sample, since the simulations assume the absence of correlation and will be unaffected by the physical separations between the lines of sight.

##### 4.2.2. Bandwidth Correction Function

The coverage of the  $\text{Ly}\alpha$  forest provided by the FOS spectra extends to within  $\approx 6 \times 10^4 \text{ km s}^{-1}$  of the emission redshift in QSO B and  $\approx 3 \times 10^4 \text{ km s}^{-1}$  in QSOs A and C. Since QSO E lies at a slightly lower redshift and the  $\text{Ly}\alpha$  forest along this sightline can only be observed up to  $z \approx 0.85$  (i.e., greater than  $3000 \text{ km s}^{-1}$  from  $z_{\text{em}}$ ), there exists a small redshift interval,  $\Delta z \approx 0.05$ , which is available along only three sightlines. This finite difference in redshift coverage between the E sightline and the other three means that more pairs may be found at smaller velocity separations than at larger ones. The effect on the velocity cross-correlations was estimated by the bandwidth correction function described by Sargent et al. (1982) in their equations (15a) and (15b). This small ( $< 10\%$ ) correction has been applied to the velocity cross-correlations calculated for the three pairs containing QSO E in the lower three panels of Figure 7.

#### 4.3. Results

Figure 7 suggests the presence of correlations between QSOs A and B in the smallest velocity bin of Samples 1 and 2. Although a few (presumably) random spikes occur among the other pairs for the various samples, no significant number of pairs above the background were seen in this particular velocity bin. The peak of eight pairs in the  $0\text{--}150 \text{ km s}^{-1}$  bin of the A/B cross-correlation of Sample 1 lines is significant at the 99.6% level assuming a Poisson distribution around the Monte Carlo expectation value of 2.50, and the six pairs of Sample 2 are significant at the 99.2% level. The decreasing number of lines in Samples 3, 4, and 5 make the velocity cross-correlation plots less interesting. Still, three pairs of lines are found in the smallest velocity bin for Samples 3 (91.4% significance) and 4 (97.4% significance). Finally, two pairs remain in Sample 5, a result significant at the 90.6% level.

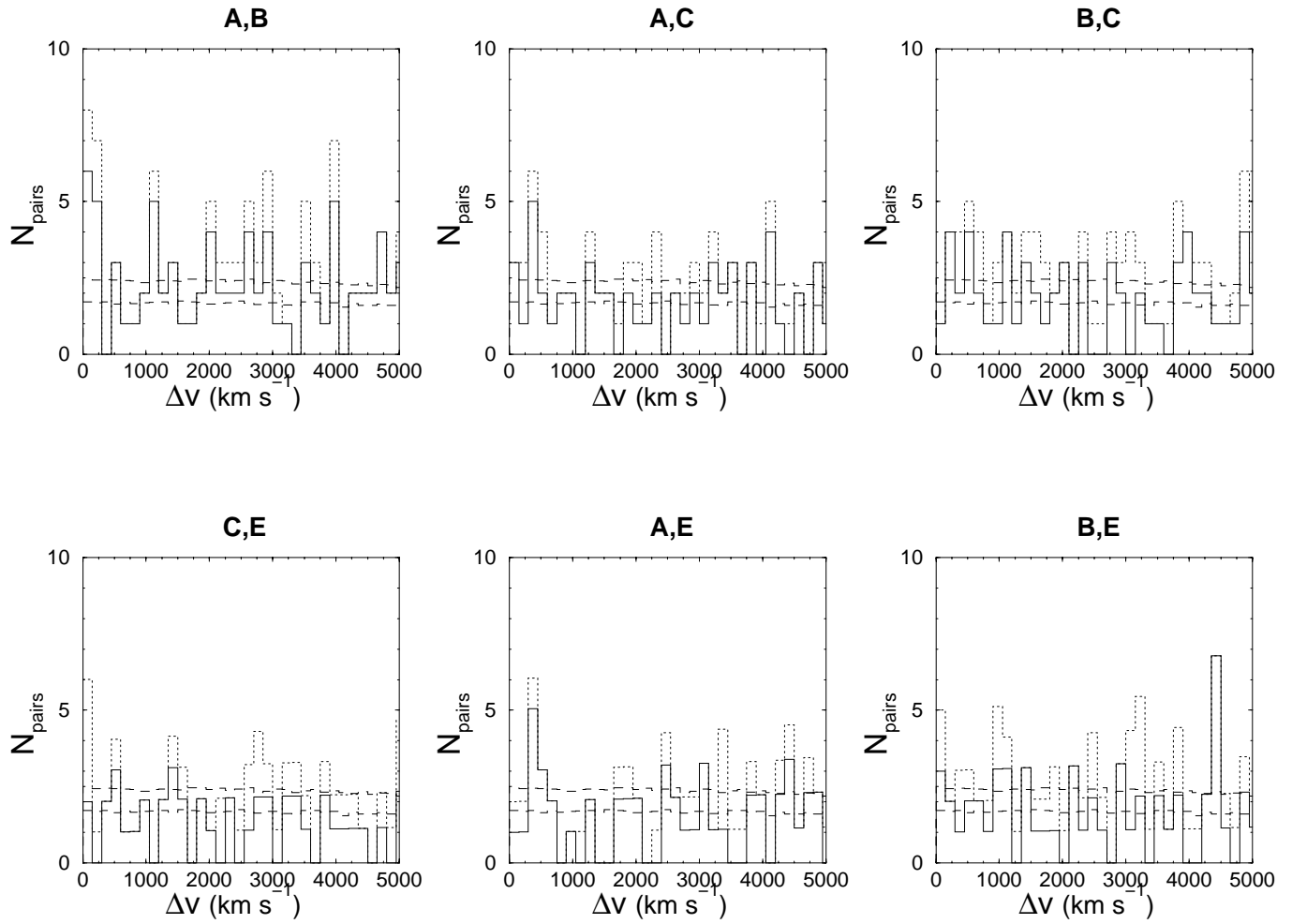


FIG. 7.—Velocity cross-correlations of Samples 1 and 2 and the corresponding random expectations. The dashed histogram is the distribution of pairs in Sample 1 ( $SL > 3.5$ ) separated by  $\Delta v < 150 \text{ km s}^{-1}$ . The upper dashed line is the random expectation from Monte Carlo simulations for uncorrelated lines of sight having the same line density as Sample 1. The solid histogram and the lower dashed line are as described above, but for Sample 2 ( $SL > 4.5$ ).

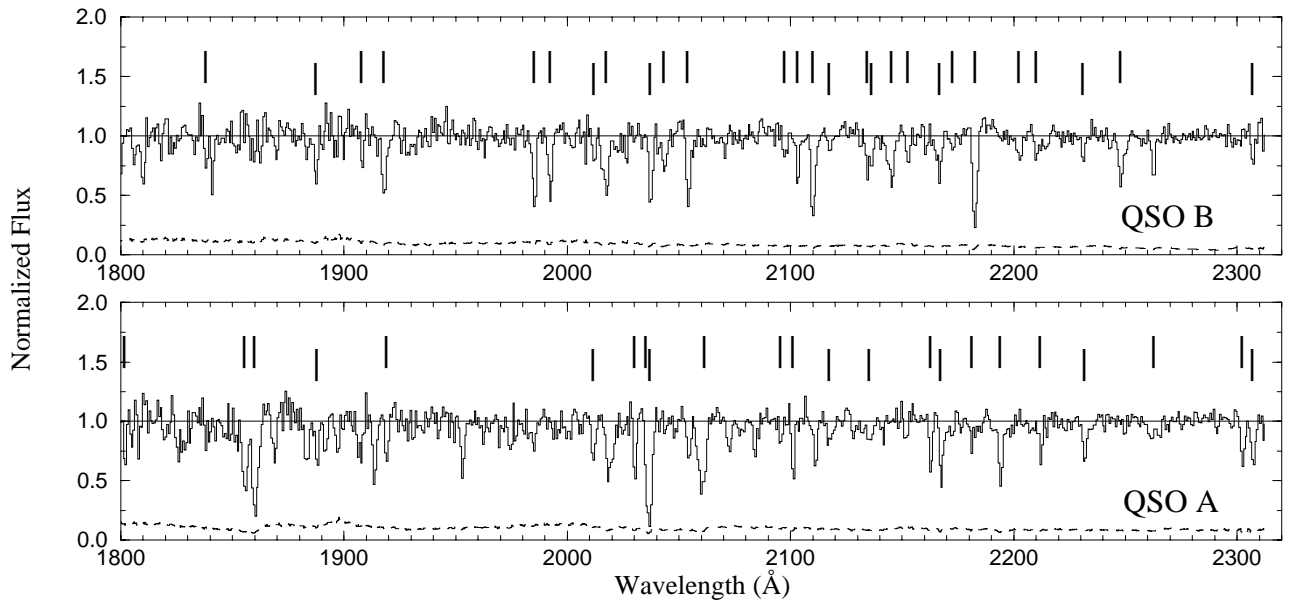


FIG. 8.—Normalized spectra of QSOs A and B, binned by 2 pixels for presentation. The tick marks indicate the lines identified as  $\text{Ly}\alpha$  forest lines with  $SL > 3.5$ ; the lower set in each panel marks the eight  $\text{Ly}\alpha$  pairs found in Sample 1.

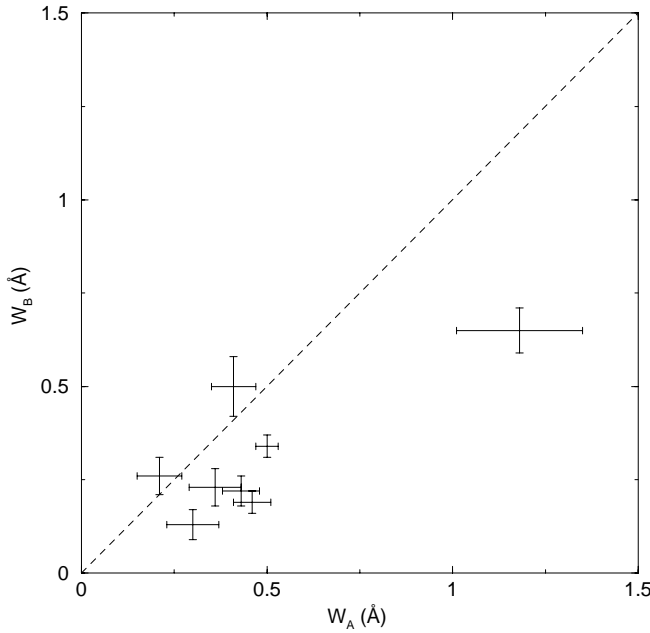


FIG. 9.—Rest equivalent widths of lines in the A/B coincidences of Sample 1.

The two-point correlation function (TPCF),  $\xi$ , defined by

$$\xi = \frac{N(\text{Obs})}{N(\text{Ran})} - 1, \quad (3)$$

can be used to describe the degree of correlation in the first bin. Here  $N(\text{Obs})$  is the observed number of pairs, and  $N(\text{Ran})$  is the random number given by the Monte Carlo simulations. In Sample 1 of the A/B pair, the eight coincidences give  $\xi = 2.2 \pm 1.1$  (errors are  $1\sigma$  standard error). Samples 2–5 have  $\xi = 2.5 \pm 1.4$ ,  $\xi = 1.9 \pm 1.7$ ,  $\xi = 3.6 \pm 2.7$ , and  $\xi = 2.9 \pm 2.8$ , respectively. The other pairs in all the samples have  $\xi < 1$ , except for Samples 3 and 4 in the B/E pair, which have  $\xi = 1.9 \pm 1.7$  and  $\xi = 2.1 \pm 2.2$ , respectively. Since these two QSOs have the widest separation (1.8 Mpc at  $z \approx 0.66$ ), these values for  $\xi$  are presumably the result of fluctuations in the small number statistics; the three pairs in Sample 3 for B/E are significant at the 91.4% level, while the three pairs in Sample 4 have a 97.4% chance of being nonrandom. Sample 1 of the C/E pair has  $\xi = 1.4 \pm 1.0$ .

#### 4.4. Equivalent Widths

The sizes and clustering properties of systems exhibiting strong Ly $\alpha$  absorption may be different from those with weaker absorption. The simulations of Charlton et al. (1997) predict that strong lines can be expected to pair off with weaker lines rather than other strong ones, a behavior that is borne out by observations (see Fang et al. 1996). On the other hand, Crofts & Fang (1998) find correlations between only the strongest lines ( $W_0 > 0.4 \text{ \AA}$ ) at  $z \approx 2.2$ . The normalized spectra of QSOs A and B are shown in Figure 8 with the coincident Ly $\alpha$  lines of Sample 1 indicated. The rest equivalent widths of these lines are plotted in Figure 9. Three of the points lie  $2\sigma$  or more away from the line of equal equivalent width, suggesting that real column density differences exist in the absorbers over scales of  $\approx 200 h^{-1} \text{ kpc}$ .

#### 5. ESTIMATION OF CORRELATION SCALE LENGTHS

The velocity cross-correlation plots demonstrate that several nonrandom coincidences of absorbers exist between the A/B pair and that there are no statistically significant pairs between either QSOs A and C at the next largest separation or in any of the other pairs. These results imply that in the transition between the two smallest separations considered here, i.e., between  $\approx 200$  and  $\approx 500 h^{-1} \text{ kpc}$ , the upper limit to the scale on which one might expect to find correlations has been reached and crossed. This dimension can translate directly into an actual absorber size or perhaps into a clustering scale length, depending on the true nature of the absorbers. Realizing that it may not ultimately be possible to distinguish between these two possibilities, we can nevertheless use the scale to obtain a general absorber size and provide a constraint on the absorber models. In this section, after calculating the physical separations between the lines of sight, we refine the size estimate by assuming two simple shapes for the absorbers—spheres and circular disks—and analytically derive the most likely radius for them using the number of coincidences and anti-coincidences in the data. We then consider constraints on filamentary structures.

The proper separation between the lines of sight as a function of angular separation on the sky in an isotropic, homogeneous universe with  $\Lambda = 0$  is

$$S = \frac{c\theta}{H_0} \frac{q_0 z + (q_0 - 1)[(1 + 2q_0 z)^{1/2} - 1]}{q_0^2(1 + z)^2}, \quad (4)$$

where  $c$  is the speed of light,  $H_0$  is the Hubble constant,  $\theta$  is the angular separation on the sky in radians, and  $q_0$  is the cosmological deceleration parameter. The six separations corresponding to the four lines of sight are presented in Table 8.

From the velocity cross-correlations, it is apparent that some correlation exists between the A/B pair on scales of  $\approx 200 h^{-1} \text{ kpc}$ , while there is no indication that the Ly $\alpha$  lines are correlated between the sightlines of the other five pairs, with separations in the range  $500 h^{-1} < S < 2000 h^{-1} \text{ kpc}$ . The number of coincident Ly $\alpha$  lines found in *all* of these other pairs is consistent with the random expectation as derived from Monte Carlo simulations. The number of lines is small enough that a very weak signal would be undetected, yet it is clear that in the transition from scales of  $\approx 200 h^{-1} \text{ kpc}$  of the A/B pair to the  $\approx 500 h^{-1} \text{ kpc}$  span, the measurable signal has disappeared. The absorber sizes have apparently reached their upper limit in this interval, and it likely lies much closer to the  $200 h^{-1} \text{ kpc}$  value. To refine the estimate it is useful to adopt some simple models

TABLE 8  
PROPER SEPARATIONS BETWEEN THE LINES OF SIGHT

QSO PAIR	$\theta$ (arcmin)	$S(q_0 = 0.5)$	
		$z_{\text{abs}} = 0.4$ ( $h^{-1} \text{ kpc}$ )	$z_{\text{abs}} = 0.9$ ( $h^{-1} \text{ kpc}$ )
A–B .....	0.98	190	248
A–C .....	2.61	504	658
B–C .....	3.20	618	807
C–E .....	5.15	994	1300
A–E .....	7.09	1370	1790
B–E .....	7.97	1540	2000

that may be unphysical but that nonetheless can provide insight. A spherical shape can be invoked for several different models of absorbers, such as “minihalos” or galaxy halos, while a flattened, circular disk may represent a galaxy (or galaxy halo); it is also a crude approximation to a sheet-like structure.

### 5.1. Spheres and Disks

Assuming the coincident lines in the A/B pair above the random expectation are real, what does that imply for the geometry of the absorbers? Going beyond a simple qualitative estimate of cloud sizes based on the line-of-sight separations requires the adoption of a specific model for the geometry of the absorbers. The idea is to choose a shape and then vary the size while estimating the probability that absorbers of that shape would be responsible for the observed pattern of absorption lines. We considered two simple shapes, spheres and disks, for which McGill (1990) developed the formalism for the probability that two lines of sight passing through them will produce pairs of lines between the spectra. D97 has adopted and extended this maximum likelihood technique, while Fang et al. (1996) used the same geometrical arguments but based their statistics on a Bayesian analysis. We used the Bayesian analysis of Fang et al. (1996) except where noted and limited ourselves in general to consideration of the A/B pair, since there is no evidence for correlated absorption between the other five pairs of QSOs having larger separations. (In § 5.2 the strength of the correlations in the A/C and B/C pairs is used to place constraints on the dimensions of possible filamentary structures by modeling them as cylinders.)

As developed by Fang et al. (1996), Bayes’s theorem can be applied to observations of pairs of QSOs to infer a posteriori the size distribution of the absorbers based on the numbers of “hits” and “misses” and a simple model for the

absorbers. A “hit” occurs when a Ly $\alpha$  absorption line exceeding the detection threshold is found in each of the two spectra within a chosen velocity window, and a “miss” is counted for each line in both spectra for which no line is seen in the opposing spectrum within that window above the detection threshold. The analysis assumes that the data are ideal, e.g., any change in SNR across the spectra can be properly accounted for. It is also assumed that all radii of spherical or disklike absorbers are equally likely to occur, and that they possess “hard” edges—the lines of sight passing through them will produce measurable absorption, but differences in the strengths of the absorption between the two lines of sight are not considered. We adopt the convention that lines in the two spectra separated by  $\leq 150$  km s $^{-1}$  are “coincident,” i.e., they arise in the same absorber, and that lines appearing in either spectrum without a corresponding line being present within 150 km s $^{-1}$  in the other spectrum are “anticoincident,” i.e., one line of sight has passed through the absorber, while the other line of sight has missed it. Although this nomenclature implies the existence of large, individual absorbers producing absorption in both spectra, the possibility also exists that the absorbers are comprised of many smaller absorbers. In the latter case, the resulting sizes could be considered a characteristic scale size for such associations. Unfortunately, such a distinction is difficult to make with our moderate resolution data.

The numbers of hits and misses were corrected for the presence of random hits by subtracting the number of random pairs from the  $N_h$  and adding twice the random pairs to  $N_m$ , since each random pair constitutes one miss in each line of sight. The probability  $\mathcal{P}(R)$  was then calculated for the cases of spheres and disks over radii of  $0 < R < 4$  h $^{-1}$  Mpc (see Fang et al. 1996). The results for spheres are shown in Table 9 and Figure 10 and for disks in Table 10

TABLE 9  
LINE COINCIDENCES IN QSOs A AND B AND SIZES OF SPHERICAL ABSORBERS FROM BAYESIAN ANALYSIS

SAMPLE	SL (lower limit)	$W_0$ (Å)	$N_{\text{hit}}$	$N_{\text{miss}}$	ABSORBER RADIUS ( $h^{-1}$ kpc)			
					Confidence Interval		Most Likely	Median
					68%	95%		
1 .....	3.5	...	5	41	152–193	140–223	164	169
2 .....	4.5	...	4	37	147–188	135–218	159	165
3 .....	5.0	0.24	2	34	134–169	125–196	132	137
4 .....	5.0	0.32	2	27	138–181	127–216	148	156
5 .....	5.0	0.40	1	24	130–169	121–204	138	146

TABLE 10  
LINE COINCIDENCES IN QSOs A AND B AND SIZES OF RANDOMLY INCLINED DISKS FROM BAYESIAN ANALYSIS

SAMPLE	SL (lower limit)	$W_0$ (Å)	$N_{\text{hit}}$	$N_{\text{miss}}$	ABSORBER RADIUS ( $h^{-1}$ kpc)			
					Confidence Interval		Most Likely	Median
					68%	95%		
1 .....	3.5	...	5	41	188–250	164–297	203	211
2 .....	4.5	...	4	37	177–242	157–289	196	205
3 .....	5.0	0.24	2	34	155–212	139–255	152	160
4 .....	5.0	0.32	2	27	161–230	142–285	179	190
5 .....	5.0	0.40	1	24	148–212	131–266	162	174

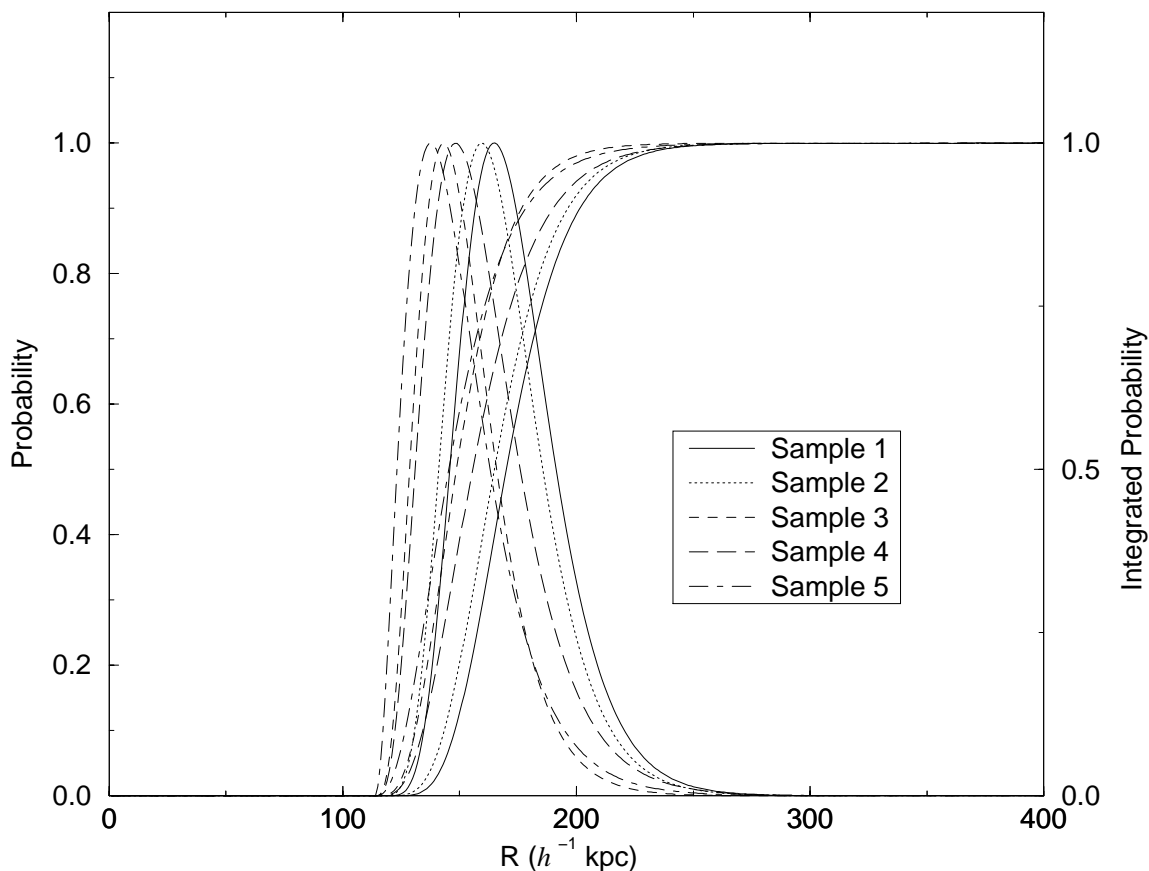


FIG. 10.—Normalized probability density function and integrated probability as a function of absorber radius as calculated from Bayes's theorem assuming spherical absorbers at  $\langle z_{\text{abs}} \rangle = 0.67$ . The five samples shown progress in strength from Sample 1, which includes all Ly $\alpha$  lines detected at greater than  $3.5 \sigma$ , through Sample 5, which includes the Ly $\alpha$  lines detected at greater than  $5.0 \sigma$  above an equivalent width cutoff of  $W_0 > 0.4 \text{ \AA}$ . Note the trend toward smaller sizes for samples of increasing line equivalent width.

and Figure 11. The sizes calculated for spheres in this way are 10%–25% smaller than for the maximum likelihood method, mainly owing to the more conservative approach of removing the random coincidences. Disks are 10%–30% smaller when the random hits are taken into account, and the smaller percentage changes occur in the larger equivalent width line samples for both spheres and disks.

### 5.2. Filaments

Another shape that arises naturally out of gravitational  $N$ -body and hydrodynamical cosmological simulations is a streaming, filamentary structure. The information gleaned from the multiple sightlines can be used to perform a test of this particular absorber shape by roughly approximating filaments as cylinders of length  $L$  and radius  $R$  and comparing the results to the observed behavior of the various QSO pairs.

The filaments were modeled using an approach adapted from Crofts & Fang (1998). A series of cylinders was stepped in  $10 h^{-1} \text{ kpc}$  increments across a grid oriented such that the  $x$ - and  $y$ -axes were aligned in the directions of right ascension and declination, respectively. The QSOs were stationary on the grid according to their positions on the sky. The cylinders themselves were constant in equivalent width, in that it was assumed that a line of sight passing through one would always produce an absorption line. To limit the computation time, the simulation was confined to consideration of only QSOs A, B, and C, since QSO E is far enough away from the other three to make the calculation

unwieldy. Despite this restriction, the placement of the QSOs on the sky (i.e., a small dispersion in right ascension, with QSO E lying nearly due north of QSO C; refer to Fig. 1), and the lack of correlation in the A/C and B/C pairs, ensures that the salient features of possible filamentary structures can be recovered from the simulation. At each point on the grid the cylinder was rotated in the plane of the sky about its minor axis through 568 positions in increments of  $0.0111$  radians, which is the angle subtended by  $2.5 h^{-1} \text{ kpc}$  at  $\langle z \rangle = 0.67$ . The radius was increased from  $25$  to  $500 h^{-1} \text{ kpc}$  for aspect ratios ( $a = L/2R$ ) of  $1$ – $10$ , corresponding to a physical range in  $L$  of  $50 h^{-1} \text{ kpc}$  to  $10 h^{-1} \text{ Mpc}$ . When a cylinder intersected the line of sight to a QSO, a hit was counted. The number of individual QSO hits was totaled for every point on the grid at each angle, radius, and aspect ratio. The size of the grid increased with the aspect ratio of the cylinders, ensuring that the cylinders are effectively started at infinity, and a natural consequence of the simulation is that the numbers of hits are equal among the QSOs, i.e.,  $N_A = N_B = N_C$ . The various incidences of two sightlines being intersected,  $N_{AB}$ ,  $N_{AC}$ , and  $N_{BC}$ , were counted, as well as the case of a hit on all three QSOs,  $N_{ABC}$ . The probabilities of obtaining hits on two or three QSOs were then calculated as  $P_{AB} = N_{AB}/N_A$ ,  $P_{AC} = N_{AC}/N_A$ ,  $P_{BC} = N_{BC}/N_B$ , and  $P_{ABC} = N_{ABC}/N_A$ .

The contours for these probabilities, samples of which are shown in Figures 12 and 13, reveal that the positions of the QSOs on the sky provide a strong constraint on the dimensions of filaments. The first thing to note from Figure 12 is

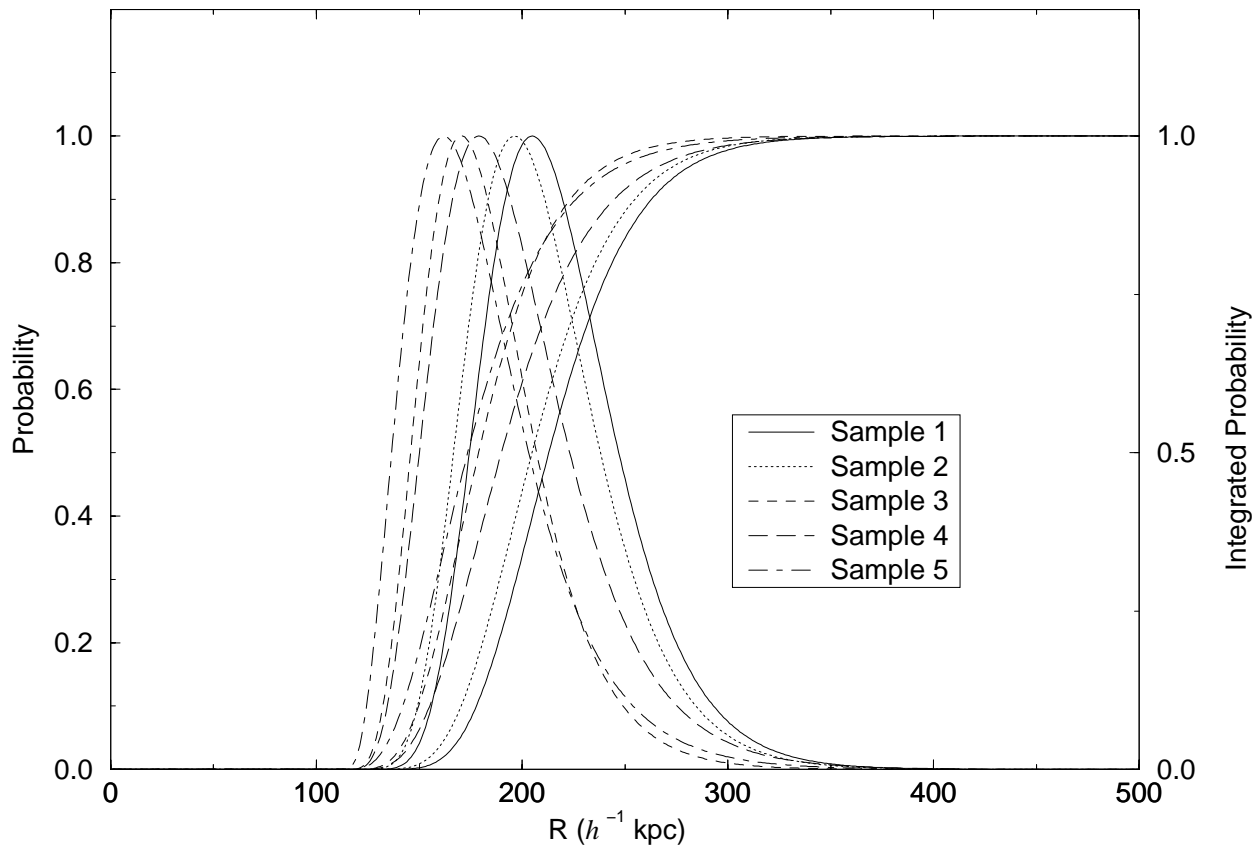


FIG. 11.— Same as Fig. 9, but for thin disks

that  $P_{AB}$  limits the radii of the cylinders to  $90 h^{-1} \lesssim R \lesssim 240 h^{-1}$  kpc. Values of  $P_{AB}$  larger than  $P_{AB} \gtrsim 0.35$  are defined only at slightly larger radii and small aspect ratios. This is because the approximately linear alignment of QSOs A, B, and C results in many three-way hits for long filaments if the filaments are aligned approximately in the

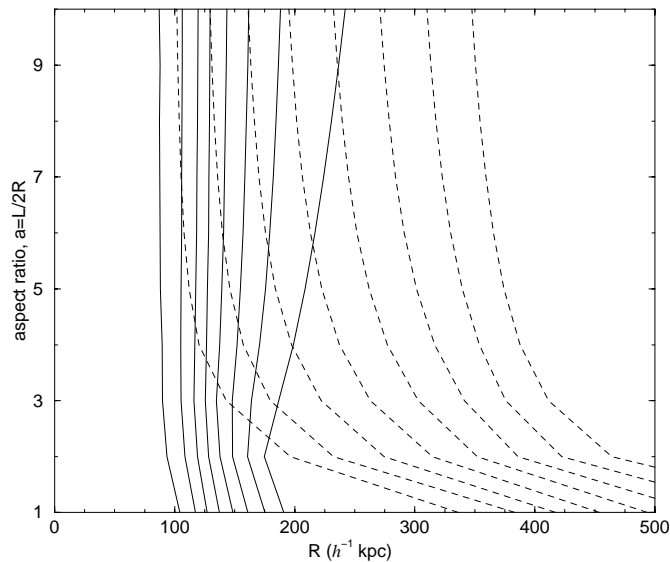


FIG. 12.—Results for the aspect ratio,  $a = L/2R$ , as a function of radius from the simulation modeling filaments as hard cylinders intersecting the QSO A and B sight lines (solid curves) and the QSO A, B, and C sight lines (dashed curves). The curves are probability contours, increasing toward larger radius, corresponding to  $P_{AB} = 0.01, 0.05, 0.10, 0.15, 0.20, 0.25, 0.30$ , and  $0.35$ ; and  $P_{ABC} = 0.01, 0.05, 0.10, 0.15, 0.20, 0.25, 0.30, 0.35$ , and  $0.40$ .

north-south direction. Therefore, most of the A and B coincidences occur across the minor axis of the cylinder, and the radius of the filaments is on the order of one-half the A/B separation. A second consequence of the alignment is that it is difficult to intersect *only* QSO B and QSO C without also intersecting QSO A, and  $P_{BC}$  is defined across the range of radii only for small values ( $P_{BC} \lesssim 0.05$ ). We exploit this characteristic below. Finally, the probability  $P_{ABC}$  is well defined at radii larger than one-half the A/B separation and over all aspect ratios (Fig. 12) but necessarily implies very large sizes.

For comparison with the simulation, the probabilities were calculated from the observed numbers of hits and misses using Sample 2. For the A/B and A/C sightlines, the number of random hits was subtracted from the observed number, and this quantity was divided by the average number of Ly $\alpha$  lines found in the two lines of sight. The errors were calculated from the 68% interval of the Poisson distribution having the observed number of pairs as its mean. No hits were found between the B/C pair, and as noted above, this is not surprising given the distribution of the QSOs. In addition, there are no cases among the Ly $\alpha$  lines of Sample 2 in which all three sightlines are intersected, i.e.,  $P_{ABC} = 0$ . The two probabilities calculable from the observations are  $P_{AB} = 0.19^{+0.16}_{-0.07}$  and  $P_{AC} = 0.06^{+0.14}_{-0.04}$ . The probability contours for three of the observational limits,  $P_{AB} = 0.12$ ,  $P_{AB} = 0.35$ , and the lower limit  $P_{AC} = 0.02$ , are plotted on Figure 13, defining three sides of a region of radii and aspect ratios in which cylinders could be found to satisfy the observations. Although a fourth observational boundary exists from the upper limit  $P_{AC} = 0.2$ , a case can be made for stronger limits from the B/C pair and/or the



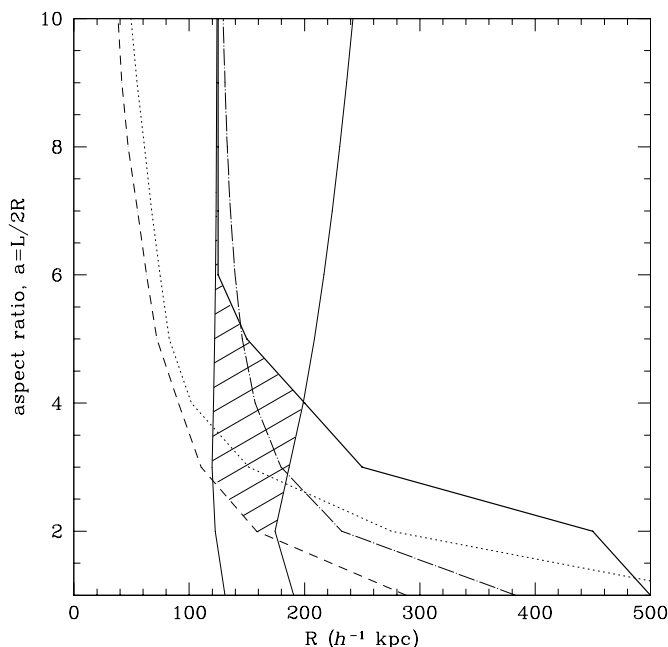


FIG. 13.—Probability contours derived from the simulation and corresponding to the  $\pm 1\sigma$  observational limits on  $P_{AB}$  (thin solid lines) and the  $1\sigma$  lower limit on  $P_{AC}$  (long-dashed line). The thick solid line is the upper limit on  $P_{BC}$  at each aspect ratio as determined from the simulation; it is an absolute upper limit on the cross-hatched region of parameter space in which cylinders could exist and exhibit the absorption line behavior observed for this QSO configuration. The  $P_{BC} = 0.02$  (short-dashed line) and  $P_{ABC} = 0.05$  (dot-dashed line) are drawn for reference.

A/B/C triplet. Although no lines were found to be in common for these last two combinations, the simulation itself provides a limit on the probability that QSOs B and C are intersected, in that  $P_{BC}$  is never greater than  $\approx 0.1$ . By using the simulation constraint for the B/C pair, at each aspect ratio on Figure 13 we have plotted the radius for which the *maximum* probability is attained at that aspect ratio. The region above this line is therefore ruled out by the simulation. The shaded area below this line and bounded by the first three observational limits is therefore the  $1\sigma$  region of parameter space that cylinders could occupy to produce the behavior observed in the correlations of lines. The cylinders found in this region would bear more than a passing resemblance to the shorter filaments (or segments of filaments) found at  $z = 0.5$  in the simulations of Davé et al. (1999).

## 6. SUMMARY AND DISCUSSION

The  $0 < v < 150 \text{ km s}^{-1}$  bin in the velocity cross-correlation between the Ly $\alpha$  absorbers of the smallest separation pair (A/B) indicates that correlations exist transverse to the line of sight over scales of  $S \approx 200 h^{-1} \text{ kpc}$ . By making the assumption that these small velocity differences imply that the lines of sight are piercing the same absorbers, we used the number of coincident and anticoincident lines to set limits on the sizes of those absorbers based on simple models. The data are not adequate to distinguish between large individual structures and correlated associations of smaller absorbers of similar global size, since the equivalent widths do not permit the itemization of individual clouds. Assuming a simple model of uniform spheres, the most likely radius predicted from the Bayesian analysis of the  $4.5\sigma$  sample of lines is  $159 h^{-1} \text{ kpc}$  with a 95% confidence

interval of  $135 h^{-1} < R < 218 h^{-1} \text{ kpc}$  for spheres, and  $R = 196 h^{-1} \text{ kpc}$  with  $157 h^{-1} < R < 289 h^{-1} \text{ kpc}$  at 95% confidence for disks. The scales inferred for spheres and disks from the correlations are more consistent with the observed sizes of individual galaxies than they are to the extents of galaxy clusters. Cylinders could also account for the observed behavior if they were of a radius comparable to the spheres and disks (i.e., on the order of the A/B separation) and a length of a few megaparsecs. Remarkably, filamentary structures with similar dimensions are seen in cosmological simulations extended to lower redshifts (e.g., Davé et al. 1999 and Riediger, Petitjean, & Mückel 1998).

As the average equivalent width of the samples in the A/B pair is increased by the elimination of weaker lines, the number of pairs observed in the  $0\text{--}150 \text{ km s}^{-1}$  bin fall off more slowly than the Monte Carlo simulations would predict based solely on the decreasing number of lines. The implication is that the cross section of the absorbers is inversely related to the strength of the line, such that higher column density systems have smaller cross sections than lower column density systems. This behavior is in agreement with the simulations of Charlton et al. (1997) and the observational result from gravitational lenses in which the heavy element systems (which contain the highest column density Ly $\alpha$  lines) exhibit differences in the Ly $\alpha$  and metal-line equivalent widths over scales of a few kpc (Smette et al. 1992, 1995; Monier et al. 1998).

There is no indication that the Ly $\alpha$  lines are correlated between the sightlines of the other five pairs that have separations in the range  $500 h^{-1} < S < 2000 h^{-1} \text{ kpc}$ . The number of coincident Ly $\alpha$  lines found in *all* of these pairs is consistent with the random expectation as derived from Monte Carlo simulations.

### 6.1. Comparison to Absorber Sizes from Previous Observations

Only one previous study of the sizes of Ly $\alpha$  absorbers has been conducted in the redshift interval  $0.4 < z < 0.9$ . The separation and size scales of the closest pair here (A/B) are very similar to those of the Q0107–025A,B pair studied by Dinshaw et al. (1995) and D97. The angular separation between those two QSOs ( $z_{\text{em}} = 0.956$  and  $0.952$ ) is  $1/29$ , which corresponds to a proper separation between the sightlines of  $270 h^{-1}$  to  $320 h^{-1} \text{ kpc}$ , i.e.,  $\approx 100 h^{-1} \text{ kpc}$  larger than the separation between QSOs A and B studied here. D97 used a maximum likelihood technique on a sample of  $5\sigma$ ,  $W_0 > 0.32 \text{ \AA}$  lines containing four pairs and six anticoincidences to estimate a characteristic radius of spherical absorbers of  $505 h^{-1} \text{ kpc}$  with 95% confidence limits of  $345 h^{-1} < R < 1520 h^{-1} \text{ kpc}$ , and a radius of  $715 h^{-1} \text{ kpc}$  with 95% limits of  $470 h^{-1} < R < 2310 h^{-1} \text{ kpc}$  for disks. A weaker line sample containing the  $5\sigma$  lines having rest equivalent widths of  $W_0 > 0.24 \text{ \AA}$  added 14 lines but no additional coincidences. The most probable radius of spherical absorbers thus decreased to  $275 h^{-1} \text{ kpc}$  with 95% limits of  $220 h^{-1} < R < 425 h^{-1} \text{ kpc}$ ; the sizes of disks were  $\approx 30\%$  larger than spheres.

A proper comparison of our results with those of D97 demands a sample of lines meeting the same criteria. We took Sample 4 and limited it to the  $\text{SNR} > 5.0$  lines in QSOs A and B in the interval  $0.48 < z < 0.89$  with rest equivalent widths of  $W_0 > 0.32 \text{ \AA}$  and no associated metal lines. This new sample met the requirements of the strong-line sample of D97. This resulted in two pairs and 21 anti-

coincident lines for which a maximum likelihood analysis (for a description, see D97) predicts a probable radius for spheres of  $R \approx 156 h^{-1}$  kpc and a 95% confidence interval of  $130 h^{-1} < R < 252 h^{-1}$  kpc, and  $145 h^{-1} < R < 340 h^{-1}$  kpc with a most likely value of  $R \approx 190 h^{-1}$  kpc for disks.

Our results for the sizes are therefore considerably smaller than those obtained by D97, which could be a result of the overly simple models. Also, this is only the second such study at these redshifts, and the analysis is sensitive to the small numbers involved, hinging on the correct identification of the Ly $\alpha$  lines. It is possible, therefore, that misidentification of some of the lines here may account for some of the discrepancy between the two results. Expanded redshift coverage and improved spectral resolution, as well as additional observations of other QSO pairs, will be needed to help to evaluate these possibilities. It is interesting to note that lowering the equivalent cutoff from 0.32 Å (Sample 4) to 0.24 Å (Sample 3) only increases the number of anticoincident lines from 25 to 32 while the number of coincidences remains at three, so that the absorber sizes inferred from Sample 3 are somewhat smaller than those for Sample 4, a behavior also noted by for D97 Q0107–025A,B. However, removing the equivalent width limit altogether reveals what we believe to be the underlying size trend in the A/B data here, namely that the absorber sizes increase with decreasing line equivalent width beyond the expectation of an increase in random pairs based solely on an increase in the number of lines.

The additional pairs formed by the four QSOs in the H1146+111 field provide a broader context in which to evaluate the A/B result for consistency. The minimum radius that spheres could possess and still span the A/C sightlines is  $\approx 250 h^{-1}$  kpc, which is at the high end of the range of values calculated for the A/B pair. It would be unlikely, therefore, to find real pairs between QSOs A and C, and in fact the velocity cross-correlation plots of Figure 7 support that conclusion; no pairs appear above the random background. Nonetheless, it is possible that apparently random pairs are in fact real, and the A/C and B/C physical separations are well within the 95% limits computed by D97. Therefore, we calculated the sizes for the best case scenario, in which *all* of the observed coincidences are real. The samples of lines in QSOs A, B, and C satisfying the D97 criteria contained *no* coincident lines in either the A/C or the B/C pairs. Using the 4.5  $\sigma$  lines of Sample 2, the predicted 95% confidence interval for spheres along the A/C sightlines is  $362 h^{-1} < R < 549 h^{-1}$  kpc with a most likely value of  $417 h^{-1}$  kpc, compared with  $404 h^{-1} < R < 756 h^{-1}$  kpc (95% confidence) and a characteristic radius of  $R \approx 501 h^{-1}$  kpc for disks. The spheres calculated in § 5.2 using the A and B coincidences of Sample 1 would have a 0.004% chance of being large enough to span the A/C separation ( $\approx 625 h^{-1}$  kpc) at  $z \approx 0.7$ , and the same probability for disks is 1.1%. This disparity between the values calculated for the A/B and A/C pairs implies either that the A/C coincidences are not real or that the absorber population possesses a wide range of sizes, only the largest of which will be detected at the A/C separation.

The separation of QSOs A and B is  $\approx 100 h^{-1}$  kpc smaller than the separation of Q0107–025A,B. Fang et al. (1996) and Crotts & Fang (1998) have found that the radii of spheres calculated using pairs of QSOs scales with QSO separation, in that the analyses of larger separation pairs result in larger predicted sizes. This effect is apparent in

Figure 10 of Crotts & Fang, who interpret it as an argument against the initial assumption of a single population of uniform spheres. (D’Odorico et al. 1998 have removed this effect by assuming a uniform prior distribution in  $R$ ). We have reproduced their Figure 14 with the addition of the result from the A/B pair (Fig. 14). The discrepancy between our measure and that of D97 at the same redshift exceeds what would be predicted based solely on the slightly larger separation of Q0107–025A,B.

The other points of Figure 14 have been obtained at higher redshifts, including two studies conducted with *HST*. Petitjean et al. (1998) used *HST*-FOS G270H data of Q1026–0045A,B ( $z_{\text{em}} = 1.438$  and 1.520, respectively) to explore scales of  $\approx 150 h^{-1}$  kpc over the redshift range  $0.83 < z < 1.44$ , from which they inferred radii of spherical absorbers ranging from  $130 h^{-1}$  kpc for a strong line sample to  $180 h^{-1}$  kpc from a sample containing weaker lines. There is apparently no difference between our measurements and those obtained by Petitjean et al. (and Crotts & Fang 1998) for Q1026–0045A,B at  $\langle z \rangle \approx 1.1$ . The second *HST* result is from the QSO pair LB 9605 (Q1517+2356,  $z_{\text{em}} = 1.834$ ) and LB 9612 (Q1517+2357,  $z_{\text{em}} = 1.898$ ), separated by  $412 h^{-1}$  kpc at  $z = 1.83$ . Here, Dinshaw et al. (1998) found five lines in common to within  $400 \text{ km s}^{-1}$  and inferred a radius for spherical absorbers of  $R \approx 380 h^{-1}$  kpc in a 95% confidence interval of  $305 h^{-1} < R < 595 h^{-1}$  kpc if all of the observed coincidences are real and arise in individual absorbers, or an upper limit of  $\approx 285 h^{-1}$  kpc to the radius if none of the coincidences are real.<sup>5</sup>

Dinshaw et al. (1998) compared their findings on the LB 9605/LB 9612 pair to the Q0107–025A,B result described above to suggest that the absorbers are evolving in size and

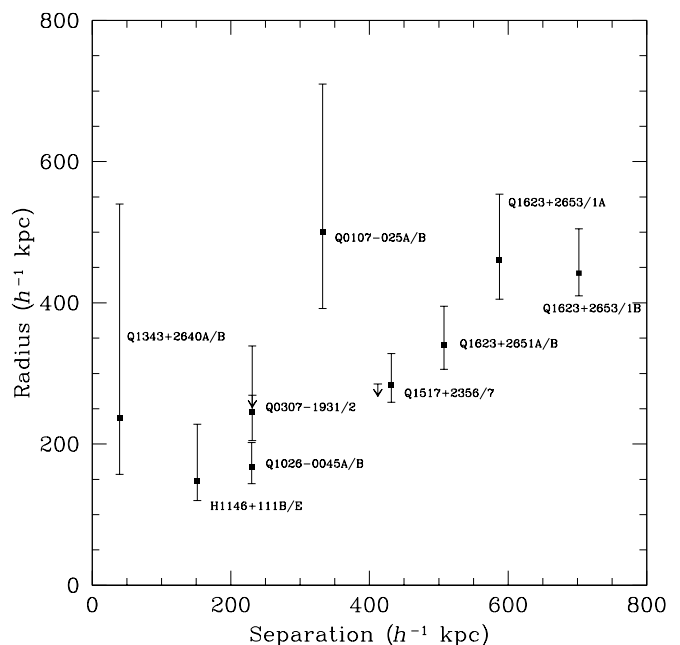


FIG. 14.—Radius of spherical absorbers as a function of the line-of-sight separation calculated for various QSO pairs, adapted from Crotts & Fang (1998), with the comparable point for the QSO A/B pair (H1146+111B/E) included from this paper.

<sup>5</sup> Crotts & Fang (1998) have analyzed these data independently and arrived at a median radius of  $283 h^{-1}$  kpc with 95% confidence upper and lower bounds of  $226 h^{-1} < R < 429 h^{-1}$  kpc.

becoming larger at lower redshifts. However, the sizes calculated here for the A/B pair, while 50% smaller than those calculated by Dinshaw et al. (1998) for the LB pair assuming all the coincidences are real, would nonetheless be in good agreement with the upper limit favored by those authors. In addition, the point at nearly the same physical separation in Figure 14 as the A/B pair is from the observations of Shaver & Robertson (1983) for the QSO pair Q0307–195A,B. These two QSOs have an angular separation of  $58''$  and lie at redshifts of  $z_{\text{em}} \approx 2$ , so that the two lines of sight subtend scales of  $240 h^{-1}$  kpc at  $\langle z \rangle \approx 1.9$ . The sizes calculated by Crotts & Fang (1998) with these data are essentially indistinguishable from those we have obtained at much lower redshifts. Recently, D'Odorico et al. (1998) obtained new ground-based spectra of this pair and calculated upper limits at 95% confidence of  $R < 269 h^{-1}$  kpc for spheres and  $R < 365 h^{-1}$  kpc for disks, in agreement with the estimate of Crotts & Fang (1998).

On the other hand, the three points from Q1623+2651A ( $z_{\text{em}} = 2.47$ ), Q1623+2651B ( $z_{\text{em}} = 2.61$ ), and Q1623+2653 ( $z_{\text{em}} = 2.53$ ), observed by Fang et al. (1996) and Crotts & Fang (1998) at  $\langle z \rangle \approx 2.2$ , cover separations equivalent to those in our A/C and B/C pairs at  $\langle z \rangle \approx 0.7$ . They found strong evidence for correlations that appear to be more pronounced among the larger equivalent width lines. Since no evidence is seen for real pairs here at the A/C separation, it is possible that the sizes of the absorbers are actually *decreasing* with redshift. This possibility is worth exploring in the context of models for the collapse of large-scale structure and galaxy formation.

Computer-generated simulations of Ly $\alpha$  clouds offer an alternate approach to interpreting the data by passing closely spaced lines of sight through the simulated clouds. Charlton et al. (1995, 1997) evolved cosmological  $N$ -body/hydrodynamical simulations to  $z = 1$  for the specific purpose of evaluating the behavior of the absorption line pairs along two lines of sight. Their analysis is limited to column densities of  $N(\text{H I}) \leq 10^{14}$  atoms  $\text{cm}^{-2}$  and so is not directly applicable to our results. This is because most of our lines at the resolution of FOS will lie on the flat part of the curve of growth and exceed  $N(\text{H I}) \approx 10^{14}$  atoms  $\text{cm}^{-2}$ , and we do not have the resolution to interpret the measured equivalent widths in terms of column densities. Nonetheless, some interesting parallels are found. Charlton et al. (1997) find that for decreasing column densities the predicted size of uniform spheres will be larger. In addition, for a given column density, the size of the spheres decreases from  $z = 3$  to  $z = 1$ , although the effect is less pronounced at the higher column densities (i.e., a factor of  $\approx 4$  for  $10^{12.5}$  atoms  $\text{cm}^{-2}$  and a factor of  $\approx 2.5$  for  $10^{14}$  atoms  $\text{cm}^{-2}$  as the redshift decreases from  $z = 3$  to  $z = 1$ ).

The results here are also in qualitative agreement with the simulations of Miralda-Escudé et al. (1996), who predict a correlation length of  $\approx 80 h^{-1}$  kpc for  $z > 2$ . This is the scale at which the number of lines involved in coincidences has decreased to one-half the value at small scales ( $\approx 10$  kpc), where nearly all of the lines are coincident. In these simulations the absorption generally arises in the gas expanding along filaments. Cen & Simcoe (1997) have extended these simulations to study the shapes and sizes of Ly $\alpha$  absorbers and the correlations between them. They argued that only observations on separation scales of  $S \lesssim 50 h^{-1}$  kpc will measure single absorbers, correlations for  $S \approx 100 h^{-1}$  kpc are due to the clustering of separate

absorbers, and any coincidences seen at  $S \approx 500 h^{-1}$  kpc are due to unrelated, uncorrelated clouds. If this behavior persists to  $z < 1$ , then in their model our results could be interpreted as favoring clustering of absorbers on  $\approx 250 h^{-1}$  kpc scales.

The approach commonly taken to look for clustering of Ly $\alpha$  absorbers along single QSO sightlines requires the calculation of the velocity autocorrelation function in a way similar to equation (1) but using the Ly $\alpha$  lines in one line of sight and the evaluation of the evidence for a signal in the bin of the smallest velocity separations that can be resolved in the spectrum. The sensitivity of the measurement to line blending and the ensuing uncertainty in the actual numbers of lines involved have meant that the clustering properties of Ly $\alpha$  forest lines have long been debated (see Rauch 1998 and references therein). At high redshift ( $z \approx 3$ ) it has been reported that there is no evidence for clustering on scales of  $300\text{--}30,000$  km  $\text{s}^{-1}$  (Sargent et al. 1980). Low values ( $\xi_r \approx 0.2$ ) of the TPCF in redshift space have been found on scales of  $\Delta v \leq 300$  km  $\text{s}^{-1}$ , and a general consensus has arisen in favor of the presence of weak clustering on small scales. However, Fernández-Soto et al. (1996) more recently used the distribution of weak C IV systems to calculate the TPCF for the Ly $\alpha$  lines and found a strikingly high value for the correlation coefficient ( $\xi_r \approx 20$ ) on scales of  $\leq 250$  km  $\text{s}^{-1}$  for Ly $\alpha$  forest clouds with  $N(\text{H I}) \geq 3 \times 10^{14}$  atoms  $\text{cm}^{-2}$ . At lower redshifts ( $z \lesssim 1.7$ ), only one study has been conducted on the clustering properties of the Ly $\alpha$  forest lines. Ulmer (1996) used *HST* QSO Absorption Line Key Project data to calculate the TPCF  $\xi_r = 1.8^{+1.6}_{-1.2}$  on scales of  $250\text{--}500$  km  $\text{s}^{-1}$  in redshift space in the interval  $0 < z < 1.3$ . This result implies that Ly $\alpha$  absorbers at low redshift have stronger clustering properties than those at high redshifts and lends support to the idea of a separate population of absorbers at lower redshifts, possibly associated with galaxies. The values calculated in § 4.3 for the TPCF may not be directly comparable to Ulmer's value because it is not known if the spatial correlation transverse to the line of sight behaves in the same way as the correlation in redshift along the line of sight. Still, the TPCF calculated for the A/B pair is consistent with the interpretation that the coincidences seen are due to the clustering of smaller absorbers, if one can assume that the spatial TPCF  $\xi_s$  is roughly equivalent to  $\xi_r$ .

## 6.2. Galaxy Halos

The sizes calculated for spherical absorbers are consistent with the prediction from the observational result that strong Ly $\alpha$  lines ( $W_0 > 0.3$  Å) at  $z_{\text{abs}} < 0.9$  arise in extended galaxy halos at impact parameters of up to  $\approx 160 h^{-1}$  kpc (Lanzetta et al. 1995; Chen et al. 1997). The estimated sizes of flattened disks are slightly larger but would also give good agreement. The cylinders occupying the parameter space defined by the simulations of § 5.2 (Fig. 13) would have sizes comparable to these large halos in at least one dimension. The spatial distribution of the halo gas in the galaxies identified as absorbers is not determined by current observations (Chen et al. 1997), and spheres and disks both remain viable candidates.

Nonetheless, the sizes we have calculated may not translate directly into halo measurements, since galaxy halos need not be the exclusive source of low- $z$  Ly $\alpha$  absorption. Although Lanzetta et al. (1995) postulate that  $\approx 30\text{--}60\%$  of all Ly $\alpha$  lines arise in large halos, there are also indications

from the strength of the galaxy-absorber correlation function that only a small fraction of Ly $\alpha$  lines arise in halos (Morris et al. 1993; Mo & Morris 1994). There is also observational evidence that Ly $\alpha$  lines, even strong ones, can arise in areas devoid of galaxies (Morris et al. 1993; Stocke et al. 1995; Tripp, Lu, & Savage 1998). In addition, it has been suggested that Ly $\alpha$  lines at low redshift may arise in tidal debris left over from galaxy interactions (Morris & van den Bergh 1993). Recent simulations of large-scale structure down to  $z = 0$  indicate that, while strong absorption lines may give the appearance of having arisen in the halos of galaxies, the effect is circumstantial and is a consequence of the fact that both galaxies and Ly $\alpha$  clouds are primarily contained in filaments. Although Ly $\alpha$  absorbers may be identified at the same redshift as galaxies, it does not necessarily follow that they are gravitationally bound to them. Therefore, an association of strong Ly $\alpha$  lines with galaxies may not be due to the existence of extended galactic halos but rather to a correlation between galaxies and Ly $\alpha$  clouds that has its origin in the fact that both galaxies and Ly $\alpha$  clouds are mostly contained in filaments.

Distinguishing among spheres, disks, and filaments is complicated by the fact that the differences in the radii predicted by these three geometries are small. Higher resolution observations could, in principle, help to determine if there is evidence for common absorption between QSOs A and C at a level that cannot currently be detected. A negative result would be enough to rule out filaments, but choosing between spheres and disks is more problematic. One approach would be to measure redshifts for galaxies in the field and identify them when possible with the Ly $\alpha$  lines in the spectra. The presence of two QSOs with galaxies in close proximity is a good test of the extended halo scenario in general.

We wish to thank Valery Khersonsky and John Hillier for helpful comments, Peg Stanley and the staff at STScI for the implementation of these observations, Don Schneider and Sofia Kirhakos for providing and assisting with the installation of the JASON software, and Eileen Kopchik for installing the necessary graphics package on the University of Pittsburgh system.

## REFERENCES

- Arp, H., & Hazard, C. 1980, *ApJ*, 240, 726  
Bahcall, J. N., et al. 1993, *ApJS*, 87, 1  
———. 1996, *ApJ*, 457, 19 (CAT2)  
Bechtold, J., Crotts, A. P. S., Duncan, R. C., & Fang, Y. 1994, *ApJ*, 437, L83  
Bechtold, J., & Yee, H. K. C. 1995, *AJ*, 110, 1984  
Blandford, R. D., Phinney, E. S., & Narayan, R. 1987, *ApJ*, 313, 28  
Cen, R., & Simcoe, R. A. 1997, *ApJ*, 483, 8  
Charlton, J. C., Anninos, P., Zhang, Y., & Norman, M. L. 1997, *ApJ*, 485, 26  
Charlton, J. C., Churchill, C. W., & Linder, S. M. 1995, *ApJ*, 452, L81  
Chen, H.-W., Lanzetta, K. M., Webb, J. K., & Barcons, X. 1997, *ApJ*, 498, 77  
Cowie, L. L., Songaila, A., Kim, T. S., & Hu, E. 1995, *AJ*, 109, 1523  
Crotts, A. P. S. 1989, *ApJ*, 336, 550  
Crotts, A. P. S., & Fang, Y. 1998, *ApJ*, 502, 16  
Davé, R., Hernquist, L., Katz, N., & Weinberg, D. H. 1999, *ApJ*, 511, 521  
Dinshaw, N., Foltz, C. B., Impey, C. D., & Weymann, R. J. 1998, *ApJ*, 494, 567  
Dinshaw, N., Foltz, C. B., Impey, C. D., Weymann, R. J., & Morris, S. L. 1995, *Nature*, 373, 223  
Dinshaw, N., & Impey, C. D. 1996, *ApJ*, 458, 73  
Dinshaw, N., Impey, C. D., Foltz, C. B., Weymann, R. J., & Chaffee, F. H. 1994, *ApJ*, 437, L87  
Dinshaw, N., Weymann, R. J., Impey, C. D., Foltz, C. B., Morris, S. L., & Ake, T. 1997, *ApJ*, 491, 45 (D97)  
D'Odorico, V., Cristiani, S., D'Odorico, S., Fontana, A., Giallongo, E., & Shaver, P. 1998, *A&A*, 339, 678  
Elowitz, R. M., Green, R. F., & Impey, C. D. 1995, *ApJ*, 440, 458  
Fang, Y., Duncan, R. C., Crotts, A. P. S., & Bechtold, J. 1996, *ApJ*, 462, 77  
Fernández-Soto, A., Lanzetta, K. M., Barcons, X., Carswell, R. F., Webb, J. K., & Yahil, A. 1996, *ApJ*, 460, L85  
Foltz, C. B., Weymann, R. J., Röser, H. J., & Chaffee, F. H. 1984, *ApJ*, 281, L1  
Hazard, C., Arp, H., & Morton, D. C. 1979, *Nature*, 282, 271  
Huchra, J. P. 1986, *Nature*, 323, 784  
Jakobsen, P., Perryman, M. A. C., Ulrich, M. H., Macchetto, F., & di Serego Alighieri, S. 1986, *ApJ*, 303, L27  
Keyes, C. D., et al. 1995, *FOS Instrument Handbook* (Baltimore: STScI)  
Lanzetta, K. M., Bowen, D. B., Tytler, D., & Webb, J. K. 1995, *ApJ*, 442, 538  
McGill, C. 1990, *MNRAS*, 242, 544  
Miralda-Escudé, J., Cen, R., Ostriker, J. P., & Rauch, M. 1996, *ApJ*, 471, 582  
Mo, H. J., & Morris, S. L. 1994, *MNRAS*, 269, 52  
Monier, E. M., Turnshek, D. A., & Lupie, O. L. 1998, *ApJ*, 496, 177  
Morris, S. L., Weymann, R. J., Dressler, A., McCarthy, P. J., Smith, B. A., Terile, R. J., Giovanelli, R., & Irwin, M. 1993, *ApJ*, 419, 524  
Morris, S. L., & van den Bergh, S. 1994, *ApJ*, 427, 696  
Ostriker, J. P., & Vishniac, E. 1986, *Nature*, 322, 804  
Paczynski, B. 1986, *Nature*, 319, 567  
Petitjean, P., Surdej, J., Smette, A., Shaver, P., Mückel, J., & Remy, M. 1998, *A&A*, 334, L45  
Petry, C. E., Impey, C. D., & Foltz, C. B. 1998, *ApJ*, 494, 60  
Phinney, E. S., & Blandford, R. D. 1986, *Nature*, 321, 569  
Rauch, M. 1998, *ARA&A*, 36, 267  
Riediger, R., Petitjean, P., & Mückel, J. P. 1998, *A&A*, 329, 30  
Sargent, W. L. W., Young, P. J., Boksenberg, A., & Tytler, D. 1980, *ApJS*, 42, 41  
Sargent, W. L. W., Young, P. J., & Schneider, D. P. 1982, *ApJ*, 256, 374  
Savage, B. D., et al. 1993, *ApJ*, 413, 116  
Schneider, D. P., et al. 1993, *ApJS*, 87, 45  
Shaver, P. A., & Cristiani, S. 1986, *Nature*, 321, 585  
Shaver, P. A., & Robertson, J. G. 1983, *ApJ*, 268, L57  
Silk, J. 1986, *Nature*, 324, 231  
Smette, A., et al. 1992, *ApJ*, 389, 39  
———. 1995, *A&AS*, 113, 199  
Stocke, J. T., Shull, J. M., Penton, S., Donahue, M., & Carilli, C. 1995, *ApJ*, 451, 24  
Tripp, T. M., Lu, L., & Savage, B. D. 1998, *ApJ*, 508, 200  
Turner, E., et al. 1986, *Nature*, 321, 142  
Ulmer, A. 1996, *ApJ*, 473, 110  
Verner, D. A., Barthel, P. D., & Tytler, D. 1994, *A&AS*, 108, 287  
Weymann, R. J., & Foltz, C. B. 1983, *ApJ*, 272, L1  
Weymann, R. J., et al. 1998, *ApJ*, 506, 1